University of Bergen

Geophysical Institute

Master Thesis in Energy

Electrical Power Engineering

Design of Grid-Tied Converter Using AFE

William Fosse

February 21, 2023

Acknowledgements

This thesis was submitted for the degree of Master of Science in the field of Energy and Electrical Power Engineering at the University of Bergen in collaboration with the Western Norway University of Applied Sciences (HVL). Facilities and resources required for the fulfilment of this thesis were provided by HVL. The work was originally carried out for the duration of the two semesters from fall 2021 to spring 2022 but partly postponed and delayed until spring 2023.

The writing of this thesis has tested me in academic challenges as well as personal ones. It has introduced me to many new fascinating aspects of electrical engineering while simultaneously pushing me to more deeply understand familiar concepts. I wish to express my sincere gratitude towards the people in my life, both personally and academically, for pushing me out of my comfort zone.

I would also like to acknowledge the counsel received from my supervisor, Associate Professor Shujun Zhang. Former master student Omes Jawaid Bajwa was a great help in the early stages of the work on this thesis, as this project is partly a continuation of the thesis submitted by him spring 2021. Senior Engineer Lars Manger Ekroll has been a huge help in both providing me with the necessary laboratory equipement and in supporting me with practical ideas. A big thanks also to Deparment Engineer Farzan Jouleh for supplying me with electronics and components for the prototype model.

Abstract

The predicted increase in electricity demand from electrification of the transportation sector has led to research of bidirectional Electric Vehicle (EV) chargers becoming an ever more popular research topic. With bidirectional chargers, power can more efficiently be transferred to EV batteries, as well as allowing energy to be transferred back to the grid or to power the household the EV is connected to during peak load hours. EV chargers of the conventional type, are typically unidirectional and thus lacking the necessary technology for bidirectional flow of current. This thesis will investigate several rectifiers and control schemes with the intent to propose an appropriate system capable of being implemented in a bidirectional EV charger. A voltage-oriented controlled active front-end rectifier is derived to fulfill this goal.

A model of the system is simulated in MATLAB Simulink in various load conditions to test the response of the controller. The simulation results show that the system is capable of transitioning from rectification during a resistive load to inversion during a regenerative load. The system is also shown to be capable of withstanding increased load, in both directions, over the intended application.

A prototype is designed for the purpose of verifying the simulated results.

Notation and Symbols

Convention of notation and list of symbols

Electrical

I,i Electrical current

V,v Voltage (Electrical potential difference)

Physical Constants

π The ratio of a circle's circumference to its diameter

e Euler's number

Superscripts

* Referance value

Subscripts

α,β Three-phase quantity projection onto two stationary axes

a,b,c Three-phase lines

d,q Rotational frame d- and q-axis components

Contents

Chapter 1

Introduction

1.1 Background

In recent years, the global energy infrastructure has been going through rapid changes. Growing concerns over climate change and degradation of the environment has strengthened the global response in favour of using renewable energy in otherwise fossil dependent sectors. The transportation sector in particular is highly dependent on fossil fuels, as almost all of the energy (over 90%) is derived from petroleum products[1].

Rapid advancements in EV technology, as well as policy changes and international treaties, such as the Paris agreement of 2015 [2] and the European Green Deal aiming for a carbon neutral Europe in 2050, has greatly increased the global EV demand[3]. As such, electrification of the transportation sector will contribute to greatly increased stresses on the electric power grid and thus the need for efficient power conversion is on the rise.

1.2 Objectives

The aim for this thesis is to design and implement a three-phase bidirectional AC/DC rectifier system at low power in order to verify control methodology and design principles scalable to higher power levels. More specifically, the objectives are:

- Propose and describe a topology.

- Build a simulation model and produce results verifying its bidirectional operation and control methodology.
- Build a prototype and measure its output for verifying the simulation results.

The rectifier system must adhere to the following specifications:

- 2kW nominal power
- 600Vdc supplied to the load
- 10kHz switching frequency
- $< 5\%$ total harmonic current distortion

Standards set by the Institute of Elecrtical and Electronics Engineers (IEEE) will serve as guidance for certain design goals, specifically a Total Harmonic Distortion (THD) of less than 5%. The standards are described in [4][5][6].

1.3 Structure

This thesis is devided into chapters: beginning with the theoretical background necessary for describing the following design, simulation, prototyping and testing of the rectifier system. LaTeXwas used for writing this thesis. Simulations, microcontroller coding and some mathematical analysis were done in MATLAB® & SIMULINK®. Figures were made in Inkscape vector graphics editor. Schematics and Printed Circuit Board (PCB) design were drawn and made using KiCad EDA.

Chapter 2

Theory

2.1 Power Semiconductor Devices

At the heart of all power converter systems are the power semiconductor devices. These devices operate in either an off-state, where current is blocked, or an on-state where current can flow. Only ideal components will have a pure on- or off-state; in all real devices there will be a small leakage current when reverse biased. All semiconductor devices can be categorized into three groups based on their degree of controllability[7].

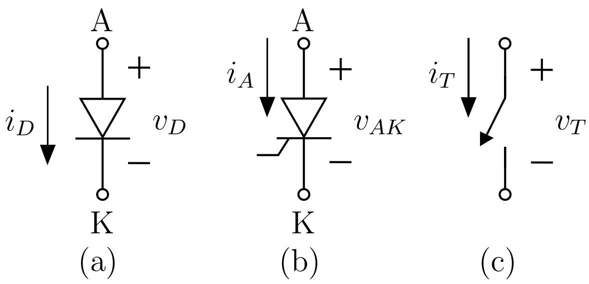

Figure 2.1: Generic semiconductor symbols for diode (a), thyristor (b) and controllable switch (c).

Diodes are wholly controled by the circuit surrounding it; the on and off states are determined by the voltage applied accross it. When forward biased, that is anode voltage higher that cathode voltage, current can flow. If reverse biased, current will be blocked. Fast recovery diodes are of interest for the application considered in this thesis. These are designed to be used in combination with controllable switches, where high-frequency currents are involved. At high power levels such diodes have reverse recovery time, t_{rr}, of less than a few microseconds[7].

A thyristor can, in its off-state, block a forward polarity voltage. The on-state can be triggered manually by applying a pulse of current at the gate terminal provided that the device is in its forward-blocking state. Once conducting, the device is latched and gate current can cease without affecting its conduction state. The thyristor can, however, not be turned off in a similar manner, meaning it will now operate as a diode until the anode current tries to go negative. Now the gate regains control of when the on-state will occur. A fully controllable switch can, however, be turned both on and off by the gate.

Among the many available controllable switches, the most popular are Bipolar Junction Transistors (BJTs), Gate Turn-off Thyristors (GTOs), Insulated Gate Bipolar Transistors (IGBTs) and Metal-Oxide-Semiconductor Field Effect Transistors (MOSFETs).

2.1.1 Comparison

Semiconductor Device	**Switching Frequency**	**Voltage Rating**	**Power Rating**
Thyristor	Lowest	Highest	Highest
GTO	Low	High	High
IGBT	High	High	Low
MOSFET	Highest	Lowest	Lowest

Table 2.1: Operating range of silicon power semiconductor devices[8].

2.2 Rectifiers

Rectifiers are used to convert ac power to dc power. The working principle of diodes and other semiconductor devices Semiconductor devices form a bridge topology connecting the ac side of the circuit to the dc bus, usually supported by a bulk capacitor[1] smoothing and securing the voltage output. Such a capacitor requires a substantial amount of energy to charge and can cause fuse breaking current spikes if not handled properly. This will be discussed in a later section (reference corrent section here).

The rectifier can work in either a single- or three-phase topology. Three-phase rectifiers are more complex in nature and more expensive but draws less current compared to a single-phase rectifier delivering the same power. In this section three-phase rectifiers will be discussed and compared. The three categories of power semiconductor devices re-

[1]The largest capacitance of a power system in parallell with the power supply. Prevents the voltage from dropping too low during short periods where current is unavailable.

spectively form three types of rectifiers: diode, thyristor and active, or fully controllable, rectifier.

2.2.1 Diode rectifier

The simplest rectifier topology is that of the diode rectifier. Current flows through the diodes according to their bias decided by the three-phase voltages applied. The top three diodes, D1, D3 and D5, are connected with common anode, and the bottom three, D2, D4 and D6, are connected with common cathode. The diodes conduct in pairs and are labeled according to when in the sequence they start and stop conducting. The sequence is D1-D2, D3-D2, D3-D4, D5-D4, D5-D6 and D1-D6, then repeating indefinetely. Each link in the sequence lasts for 60°. One full sequence therefore consists of six voltage peak pulses for the full period of 360°, all diodes each conducting for 120°.

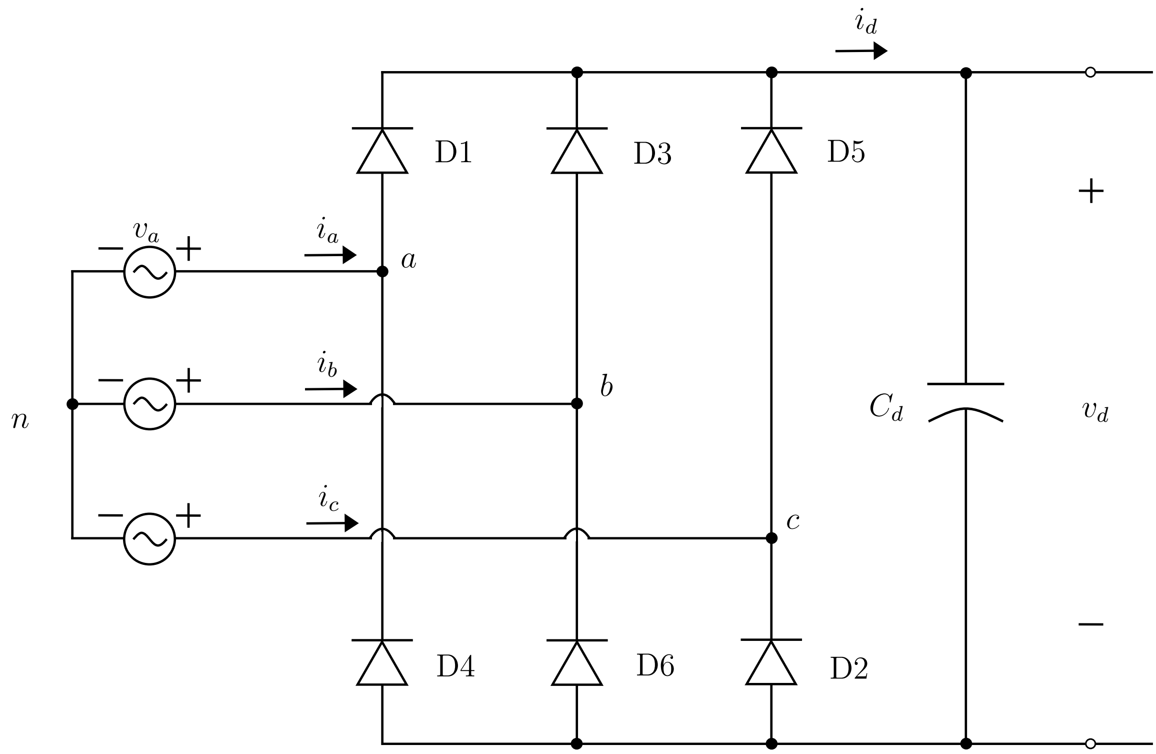

Figure 2.2: Three-phase diode rectifier.

Instantaneous voltage output:

$$v_d = v_{ab} = \sqrt{2}V_{LL}\cos\omega t \qquad -\frac{1}{6}\pi < \omega t < \frac{1}{6}\pi \tag{2.1}$$

$$V_d = \frac{1}{\pi/3}\int_{-\pi/6}^{\pi/6} \sqrt{2}V_{LL}\cos\omega t\, d\omega t = \frac{3}{\pi}\sqrt{2}V_{LL} \approx 1.35V_{LL} \tag{2.2}$$

The root-mean-square (rms) value of the line current.

$$I_s = \sqrt{\frac{1}{2\pi}\int_0^{2\pi} I_d^2\, d\omega t} = \sqrt{\frac{2}{3}}I_d {\approx} 0.816 I_d \tag{2.3}$$

By means of Fourier analysis if i_s in this idealized case, the fundamental-frequency component i_{s1} has rms value

$$I_{s1} = \frac{1}{\pi}\sqrt{6}I_d {\approx} 0.78 I_d \tag{2.4}$$

Since i_{s1} is in phase with supply voltage $DPF = 1.0$, therefore the power factor and current distortion is as follows.

$$PF = \frac{I_{s1}}{I_s}\cos\phi = \frac{3}{\pi}{\approx}0.955 \tag{2.5a}$$

$$THD_i = \frac{\sqrt{I_s^2 - I_{s1}^2}}{I_{s1}}{\times}100\%{\approx}31.08\% \tag{2.5b}$$

2.2.2 Thyristor rectifier

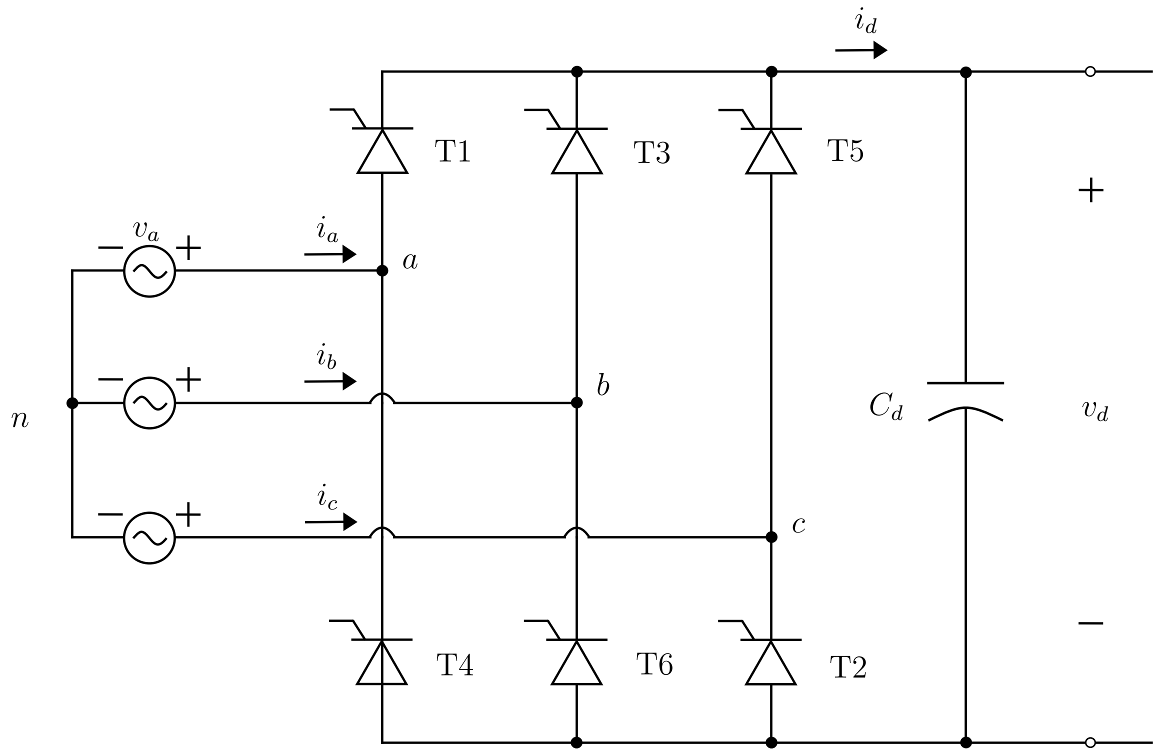

Figure 2.3: Three-phase thyristor rectifier.

$$V_{d\alpha} = V_d - \frac{A_\alpha}{\pi/3} \tag{2.6}$$

$$v_{ac} = \sqrt{2}V_{LL}\cos\omega t \tag{2.7}$$

The volt-second area A_α

$$A_\alpha = \int_0^\alpha \sqrt{2}V_{LL}\cos\omega t\, d\omega t = \sqrt{2}V_{LL}(1-\cos\alpha) \tag{2.8}$$

Substituting A_α into eq. (2.6) using eq. (2.2) for V_d:

$$V_{d\alpha} = \frac{3\sqrt{2}}{\pi}V_{LL}\cos\alpha \approx 1.35V_{LL}\cos\alpha \tag{2.9}$$

Line current is the same as for the diode rectifier.

$$I_s = \sqrt{\frac{2}{3}}I_d{\approx}0.816I_d \tag{2.10a}$$

$$I_{s1} = \frac{1}{\pi}\sqrt{6}I_d{\approx}0.78I_d \tag{2.10b}$$

Displacement angle $\phi = \alpha$, such that $DPF = \cos\alpha$, therefore

$$PF = \frac{I_{s1}}{I_s}\cos\phi = \frac{3}{\pi}\cos\alpha{\approx}0.955\cos\alpha \tag{2.11a}$$

$$THD_i = \frac{\sqrt{I_s^2 - I_{s1}^2}}{I_{s1}}{\times}100\%{\approx}31.08\% \tag{2.11b}$$

2.2.3 Active rectifier

An active rectifier, also called an Active Front End (AFE) converter, overcomes the control limitations of diode and thyristor rectifiers. This allows forced commutation between semiconductors.

2.2.4 Comparison

Recctifier	**Control**	**PF**	**THD$_i$**
Diode	None	Low	High
Thyristor	Half	Low	High
Active	Full	High	Low

Table 2.2: Comparison of different rectifier systems.

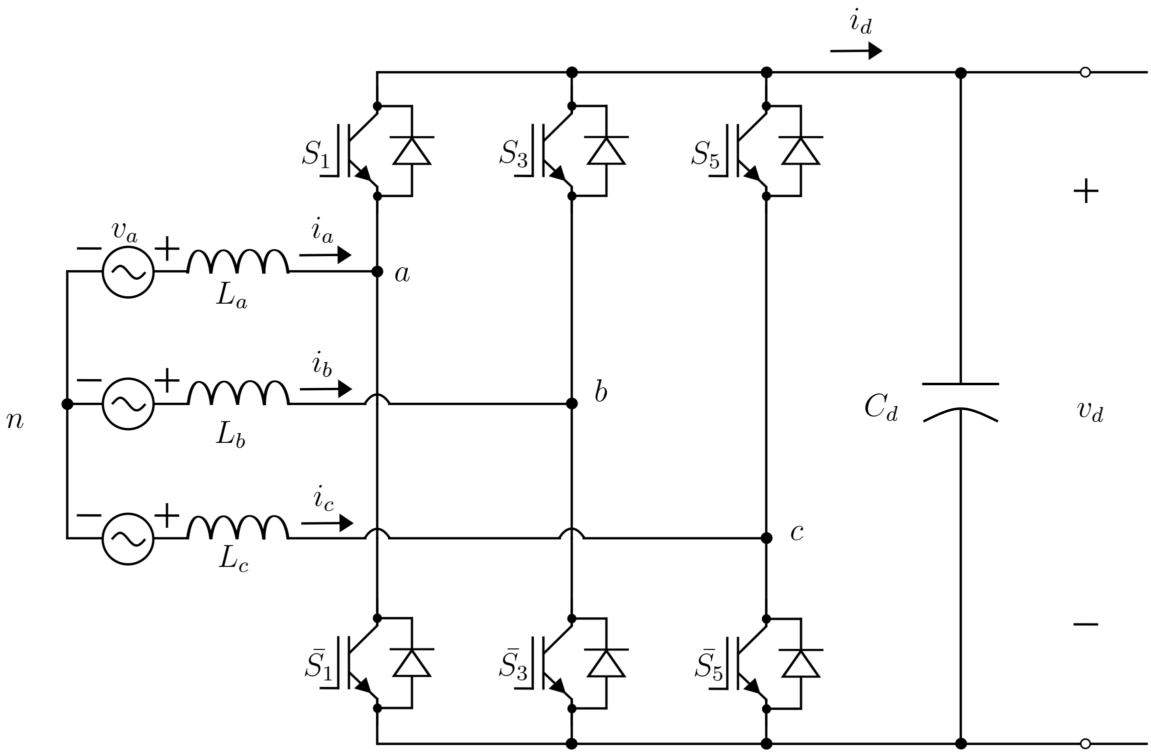

Figure 2.4: Three-phase active rectifier with IGBTs.

2.3 Control Methodology

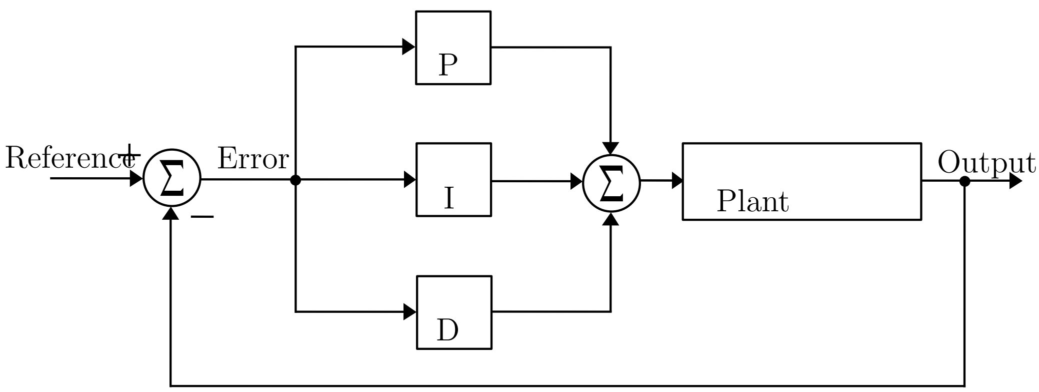

Figure 2.5: PID controller block diagram.

PID Gain	%-Overshoot	Settling Time	Steady-State Error
Increasing K_p	Increases	Min. impact	Decreases
Increasing K_i	Increases	Increases	Zero steady-state error
Increasing K_d	Decreases	Decreases	No impact

Table 2.3: Effect of increasing the PID gains on the step response.

2.3.1 PID Controllers

2.3.2 Park- and Clarke-transform

The signals we are measuring and feeding into our control system are three-phase sinusoidal ac-signals. These are highly complex and complicated to control. By simplifying into more manageable quantities two things are acheived; the system is controllable by simpler methods and the control software will be slimmer allowing for faster more reliable code.

There are two key coordinate transformations; the Clarke- and Park-transform. After processing through both transformations and regulators the inverse transform can then be applied, thus returning the signals to three-phase ac values.

Clarke transformation:

$$\boldsymbol{I}_{\alpha\beta 0} = \boldsymbol{T}_C \boldsymbol{I}_{abc} = \underbrace{\frac{2}{3}\begin{bmatrix} 1 & -\frac{1}{2} & -\frac{1}{2} \\ 0 & \frac{\sqrt{3}}{2} & -\frac{\sqrt{3}}{2} \\ \frac{1}{2} & \frac{1}{2} & \frac{1}{2} \end{bmatrix}}_{T_{abc\to\alpha\beta 0}} \begin{bmatrix} I_a \\ I_b \\ I_c \end{bmatrix} \tag{2.12}$$

Power invariant Clarke transformation:

$$\boldsymbol{I}_{\alpha\beta 0} = \boldsymbol{T}_C \boldsymbol{I}_{abc} = \underbrace{\sqrt{\frac{2}{3}}\begin{bmatrix} 1 & -\frac{1}{2} & -\frac{1}{2} \\ 0 & \frac{\sqrt{3}}{2} & -\frac{\sqrt{3}}{2} \\ \sqrt{\frac{1}{2}} & \sqrt{\frac{1}{2}} & \sqrt{\frac{1}{2}} \end{bmatrix}}_{T_{abc\to\alpha\beta 0}} \begin{bmatrix} I_a \\ I_b \\ I_c \end{bmatrix} \tag{2.13}$$

Inverse Clarke transformation:

$$\boldsymbol{I}_{abc} = \boldsymbol{T}_C^{-1} \boldsymbol{I}_{\alpha\beta 0} = \underbrace{\sqrt{\frac{2}{3}}\begin{bmatrix} 1 & 0 & \frac{1}{\sqrt{2}} \\ -\frac{1}{2} & \frac{\sqrt{3}}{2} & \frac{1}{\sqrt{2}} \\ -\frac{1}{2} & -\frac{\sqrt{3}}{2} & \frac{1}{\sqrt{2}} \end{bmatrix}}_{T_{\alpha\beta 0\to abc}} \begin{bmatrix} I_\alpha \\ I_\beta \\ I_0 \end{bmatrix} \tag{2.14}$$

Park transformation:

$$\boldsymbol{I}_{dq0} = \boldsymbol{T}_P \boldsymbol{I}_{\alpha\beta 0} = \underbrace{\begin{bmatrix} \cos\theta & \sin\theta & 0 \\ -\sin\theta & \cos\theta & 0 \\ 0 & 0 & 1 \end{bmatrix}}_{T_{\alpha\beta 0 \to dq0}} \begin{bmatrix} I_\alpha \\ I_\beta \\ I_0 \end{bmatrix} \tag{2.15}$$

[9]Combined Clarke and Park transformation matrix:

$$\boldsymbol{T}_{CP} = \boldsymbol{T}_C \boldsymbol{T}_P = \underbrace{\sqrt{\frac{2}{3}} \begin{bmatrix} \cos\theta & \cos(\theta - \frac{2\pi}{3}) & \cos(\theta + \frac{2\pi}{3}) \\ -\sin\theta & -\sin(\theta - \frac{2\pi}{3}) & -\sin(\theta + \frac{2\pi}{3}) \\ \sqrt{\frac{1}{2}} & \sqrt{\frac{1}{2}} & \sqrt{\frac{1}{2}} \end{bmatrix}}_{T_{abc \to dq0}} \tag{2.16}$$

Inverse Clarke and Park transformation matrix:

$$\boldsymbol{T}_{CP}^{-1} = \underbrace{\sqrt{\frac{2}{3}} \begin{bmatrix} \cos\theta & -\sin\theta & \sqrt{\frac{1}{2}} \\ \cos(\theta - \frac{2\pi}{3}) & -\sin(\theta - \frac{2\pi}{3}) & \sqrt{\frac{1}{2}} \\ \cos(\theta + \frac{2\pi}{3}) & -\sin(\theta + \frac{2\pi}{3}) & \sqrt{\frac{1}{2}} \end{bmatrix}}_{T_{dq0 \to abc}} \tag{2.17}$$

2.4 Harmonic Distortion

2.4.1 Filtering

L-filter

Poses higher impedance for higher frequency currents. Providing $-20dB/dec$ attenuation.

LC-filter

Poses higher impedance for higher frequency currents as well as a short circuit path to ground through the filter capacitor. Providing $-40dB/dec$ attenuation.

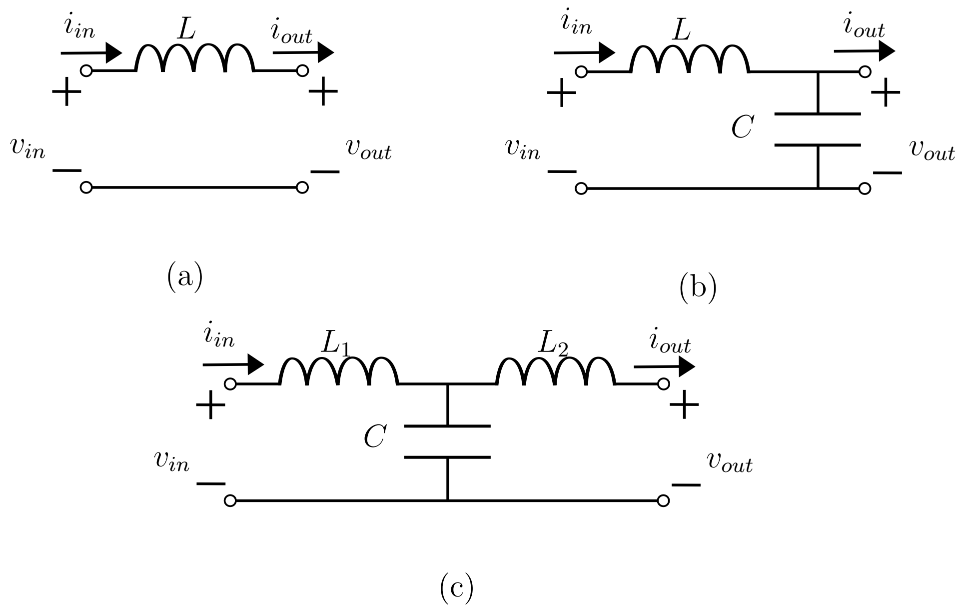

Figure 2.6: Passive filters. L-filter (a), LC-filter (b) and LCL-filter (c).

LCL-filter

Poses an even higher impedance for higher frequency currents as well as a short circuit path to ground through the filter capacitor. Providing $-60dB/dec$ attenuation.

Chapter 3

Design

The following chapter presents the proposed design for the rectifier system. Based on the therotical framework outlined in the previous chapter, the design methodology aims to satisfy the specifications for the rectifier given in Section 1.2.

To satisfy the need for bidirectional flow of energy, an AFE recifier is needed. This entails the need for controllable switches and an appropriate control scheme to drive their gates. Power transistors used in switch-mode[1] must be driven by Pulse-Width-Modulation (PWM) signals. Of the two common types discussed in **??**, Space-Vector Pulse-Width-Modulation (SV-PWM) allows for better utilization of the DC bus voltage. The additional computing required compared to Sinusoidal Pulse-Width-Modulation (S-PWM) is made up for by powerful modern Microcontroller Units (MCUs).

In order to mitigate harmonics, an LCL-filter is used. This ensures smaller filter inductors leading to lower THD and higher efficiency. Choosing an LCL-filter over a simple L-filter, or even an LC-filter, leads to higher complexity of the control scheme and possible instability due to filter resonance. The apparent higher complexity can be worked around by applying a simplification discussed in the follwing section. As presented in Section 2.4.1, the risk of instability by resonance can be lowered by either passive or active damping. The extra losses associated with passive damping resistors and the additional active damping control algorithms, pose some difficulties. However, it is possible to obtain stability without damping [source]. Therefore an undamped filter design will be used.

The two most common control schemes for voltage source converters are Voltage Oriented Control (VOC) and Direct Power Control (DPC). DPC seems to be the least complicated

[1]In switch-mode the power transistors are either completely off, no current flowing, or fully on with all availiable current flowing.

of the two, due to it not using coordinate transformation or current control loops. On the other hand, DPC is prone to high estimation errors. VOC is capable of gaining lower THD while requiring lower a sampling rate making it more reliable [source]. For these reasons, VOC is the preferred control scheme for this thesis. Laying the groundwork for the implementation of VOC is the mathematical model of the rectifier system.

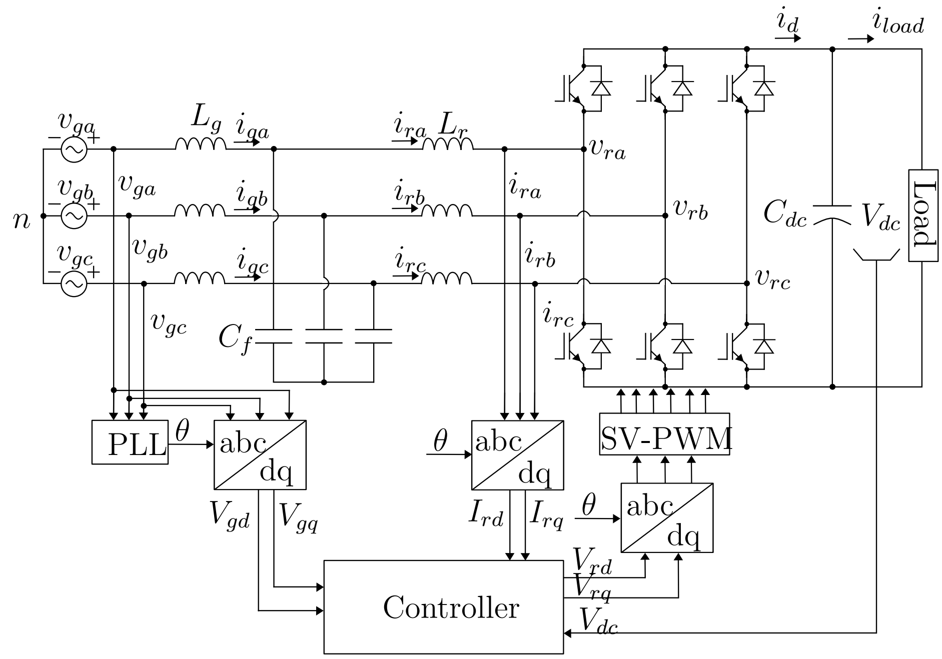

Figure 3.1: Proposed topology of the rectifier.

3.1 Mathematical Model

In a balanced three-phase symstem $i_a + i_b + i_c = 0$. Space vector representation of the three-phase voltages and currents can be defined as in eq. (3.1) and eq. (3.2) respectively[Ned mohan Electric Drives chap 9.4].

$$\boldsymbol{v}(t) = v_a(t) + v_b(t)e^{j2\pi/3} + v_c(t)e^{j4\pi/3} \tag{3.1}$$

$$\boldsymbol{i}(t) = i_a(t) + i_b(t)e^{j2\pi/3} + i_c(t)e^{j4\pi/3} \tag{3.2}$$

Phase a is chosen as the reference axis with an angle of $0°$, where phase b and c are rotated $e^{j2\pi/3} = 120°$ and $e^{j2\pi/3} = 240°$ respectively. Differential equations of the LCL-filter in stationary reference frame in space vector terms can be derived as eqs. (3.3)–(3.5).

$$L_g \frac{d\boldsymbol{i}_g}{dt} = \boldsymbol{v}_g - \boldsymbol{v}_{c_f} - (R_g + R_c)\boldsymbol{i}_g + R_c\boldsymbol{i}_r \tag{3.3}$$

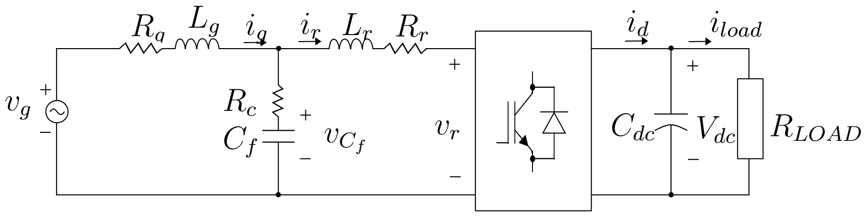

Figure 3.2: Single-phase equivalent circuit.

and

$$L_r \frac{d\boldsymbol{i}_r}{dt} = \boldsymbol{v}_{c_f} - \boldsymbol{v}_r - (R_r + R_c)\boldsymbol{i}_r + R_c \boldsymbol{i}_g \tag{3.4}$$

and

$$C_f \frac{d\boldsymbol{v}_{c_f}}{dt} = \boldsymbol{i}_g - \boldsymbol{i}_r \tag{3.5}$$

L_g being the grid-side filter inductor, L_r the rectifier-side filter inductor and C_f the filter capacitor. R_g and R_r is resistance of the wires and the inductor coil wire on the grid- and rectifier-side respectively. R_c is the Equivalent Series Resistance (esr) of the filter capacitor.

Then the rotational dq-frame voltages can be derived by first considering a set of orthogonal $\alpha\beta$ stationary frame voltages The two coordinate systems relate by $\boldsymbol{v}_{\alpha\beta} = \boldsymbol{v}_{dq} e^{j\omega t}$. The $\alpha\beta$-voltages are created by respectively combining eqs. (3.3)–(3.4) with an equal set of eqs. (3.3)–(3.4) multiplied on both sides by the operator j. This results in a new set of eqs. (3.6)–(3.7) where $\boldsymbol{v}_{\alpha\beta} = v_\alpha + jv_\beta$ and similarily $\boldsymbol{i}_{\alpha\beta} = i_\alpha + ji_\beta$:

$$L_g \frac{d\boldsymbol{i}_{g\alpha\beta}}{dt} = \boldsymbol{v}_{g\alpha\beta} - \boldsymbol{v}_{c_f\alpha\beta} - (R_g + R_c)\boldsymbol{i}_{g\alpha\beta} + R_c \boldsymbol{i}_{r\alpha\beta} \tag{3.6}$$

and

$$L_r \frac{d\boldsymbol{i}_{r\alpha\beta}}{dt} = \boldsymbol{v}_{c_f\alpha\beta} - \boldsymbol{v}_{r\alpha\beta} - (R_r + R_c)\boldsymbol{i}_{r\alpha\beta} + R_c \boldsymbol{i}_{g\alpha\beta} \tag{3.7}$$

$$\boldsymbol{v}_{g\alpha\beta} = \boldsymbol{v}_{gdq} e^{j\omega t} \tag{3.8a}$$
$$\boldsymbol{v}_{r\alpha\beta} = \boldsymbol{v}_{rdq} e^{j\omega t} \tag{3.8b}$$
$$\boldsymbol{i}_{g\alpha\beta} = \boldsymbol{i}_{gdq} e^{j\omega t} \tag{3.8c}$$
$$\boldsymbol{i}_{r\alpha\beta} = \boldsymbol{i}_{rdq} e^{j\omega t} \tag{3.8d}$$
$$\boldsymbol{v}_{c_f\alpha\beta} = \boldsymbol{v}_{c_fdq} e^{j\omega t} \tag{3.8e}$$

Substituting the expressions from eqs. (3.8a)–(3.8e) into eqs. (3.6)–(3.7) gives the voltages in the rotational frame. From there the real and imaginary components can be separated resulting in eqs. (3.9)–(3.12), two complimentary sets of the d- and q-axis voltages:

d-axis:

$$L_g \frac{di_{gd}}{dt} = v_{gd} - v_{c_f d} - (R_g + R_c) i_{gd} + R_c i_{rd} + \omega L_g i_{gq} \tag{3.9}$$

and

$$L_r \frac{di_{rd}}{dt} = v_{c_f d} - v_{rd} - (R_r + R_c) i_{rd} + R_c i_{gd} + \omega L_r i_{rq} \tag{3.10}$$

q-axis:

$$L_g \frac{di_{gq}}{dt} = v_{gq} - v_{c_f q} - (R_g + R_c) i_{gq} + R_c i_{rq} - \omega L_g i_{gd} \tag{3.11}$$

and

$$L_r \frac{di_{rq}}{dt} = v_{c_f q} - v_{rq} - (R_r + R_c) i_{rq} + R_c i_{gq} - \omega L_r i_{rd} \tag{3.12}$$

The same procedure can be followed for the current relation, resulting in eqs. (3.13)–(3.14).

d-axis:

$$C_f \frac{dv_{c_f d}}{dt} = i_{gd} - i_{rd} + \omega C_f v_{c_f q} \tag{3.13}$$

q-axis:

$$C_f \frac{dv_{c_f q}}{dt} = i_{gq} - i_{rq} - \omega C_f v_{c_f d} \tag{3.14}$$

Doing a Łaplace transform on the resulting d- and q-axis equations gives the response in transfer function terms:

$$V_{gd} = (R_g + R_c + sL_g) I_{gd} + V_{c_f d} - \omega L_g I_{gq} - R_c Ird \tag{3.15a}$$

$$V_{rd} = V_{c_f d} - (R_r + R_c + sL_r) I_{rd} + \omega L_r I_{rq} + R_c Igd \tag{3.15b}$$

$$sC_f V_{c_f d} = I_{gd} - Ird + \omega C_f V_{c_f q} \tag{3.15c}$$

$$V_{gq} = (R_g + R_c + sL_g) I_{gq} + V_{c_f q} + \omega L_g I_{gd} - R_c Irq \tag{3.15d}$$

$$V_{rq} = V_{c_f q} - (R_r + R_c + sL_r) I_{rq} - \omega L_r I_{rd} + R_c Igq \tag{3.15e}$$

$$sC_f V_{c_f q} = I_{gq} - Irq - \omega C_f V_{c_f d} \tag{3.15f}$$

Adapting eqs. (3.9)–(3.15f) into a blockdiagram - see Figure 3.3 - allows a simpler means of extracting the system transfer functions of interest to this thesis.

Several steps of blockdiagram reduction finally produces the desired transfer function of I_{rd}/V_{gd}.

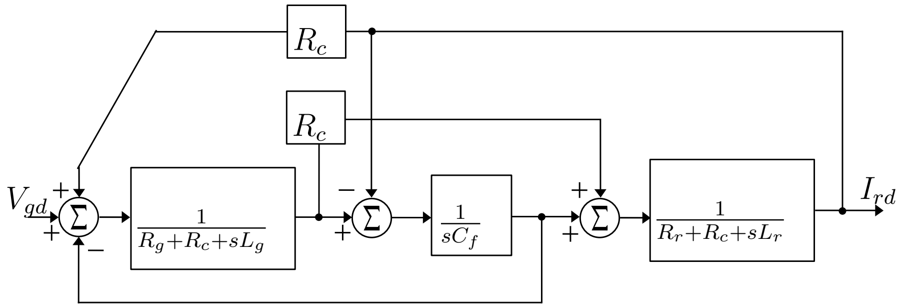

Figure 3.3: Blockdiagram of the systems mathematical model.

$$\frac{I_{rd}}{V_{gd}} = \frac{sC_fR_c + 1}{s^3C_fL_gL_r + s^2C_f[L_g(R_r + R_c) + L_r(R_g + R_c)] + s[C_f(R_gR_r + R_gR_c + R_rR_c) + L_g + L_r] + R_g + R_r} \tag{3.16}$$

A simplification can be considered. The parallell filter capacitor poses a huge impedance at the operative frequenncy, while providing a short to ground for the high-frequency noise. Therefore, for control purposes, the capacitor can be neglected. Following the same procedure as before to discover the transfer function of I_{rd}/V_{gd}. A much simpler set of two voltage equations is aquired. Skipping the in-between steps straight to the frequency-domain.

$$V_{gd} = (R_{tot} + sL_{tot})I_{rd} - \omega L_{tot}I_{rq} + V_{rd} \tag{3.17a}$$

$$V_{gq} = \underbrace{(R_{tot} + sL_{tot})I_{rq}}_{\text{voltage drop}} + \underbrace{\omega L_{tot}I_{rd}}_{\text{decoupling term}} + V_{rq} \tag{3.17b}$$

Equations (3.17a)–(3.17b) contains the supply voltage term, the voltage on the rectifier

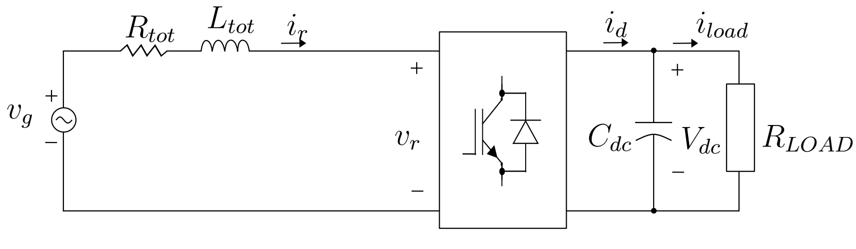

Figure 3.4: Simplified single-phase equivalent circuit.

bridge, a voltage drop term and a decoupling term. Working these into a transfer function gives:

$$\frac{I_{rd}}{V_{gd}} = \frac{1}{R_{tot} + sL_{tot}} \tag{3.18}$$

The high frequency noise filter designed for this project [10]. Phase-Locked Loop (PLL)

In order to streamline the rest of this section on the design process, an outline of the main components chosen for the prototype will now be presented.

3.1.1 Signal Propagation

A single gating signal must pass through several stages from the software generating it to the end goal of the IGBT gate-terminal. At each junction a few conditions must be met to ensure proper propagation of the pulse. These conditions follow from the specifications of the separate stages. The MCU chosen for this project, the TI LAUNCHXL-F28379D, is capable of supplying 3.3V through an internal DC/DC converter

OptoCoupler

Removing electrical noise from signals. Isolating low-voltage devices from high-voltage circuits. Allow small digital signals to control larger ac-voltages. An optically coupled Light Emitting Diode (LED) and phototransistor.

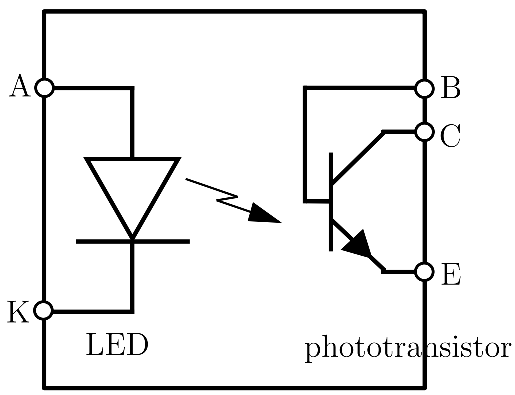

Figure 3.5: OptoCoupler schematic.

Chapter 4

Simulation Model

MATLAB®Simulink®is used to build the complete rectifier system in a blockdiagram based simulation environment. This chapter will serve to present the model of the rectifier system and all its components, while simulation results will be presented later in Chapter 6 on tests and results. Simulations in this environment can be conducted in the discrete or continuous domain. A sufficiently small sample time of $1\mu s$ is chosen, thus allowing 100 calculation per switching cycle of $1/f_s = 1/10kHz = 0.1ms$ while not being overly demanding on computing power. The sample time is entered into the powergui block configured in the discrete domain. The simulation solver, found under model configuration parameters, is set to be fixed-step discrete with the same sample time of $1\mu s$. The fixed-step discrete solver is chosen to disallow continuous states. This will make the software compatible with a real-life MCU such as the TI-Launchpad used for this thesis, making it easier later to adapt and deploy the control algorithm to hardware. Sample time within all blocks is chosen as -1, which indicates that the sample time will be *inherited* and Simulink determines an appropriate sample time for the block. For deployment to real-time hardware the sample times must be individually lowered to appropriate levels to allow more effiecently running code and to not overload the processor. For the purpose of presenting and verifying the control algorithms, this method of analysis under ideal conditions is acceptable. All algorithms are implemented with written MATLAB functions or with availiable prebuilt Simulink library blocks. An overview of the Simulink model can be seen in Figure 4.1.

The model consists of the main circuit with source and load, PLL and coordinate transform, regulator and SV-PWM generator. There is also a radiobutton for choosing to ground all gate signals to allow diode rectifier operation. The color of the blocks denote common sample time. The model is designed to provide a steady DC voltage to the load while maintaining Unity Power Factor (UPF) in closed loop operation. The controller

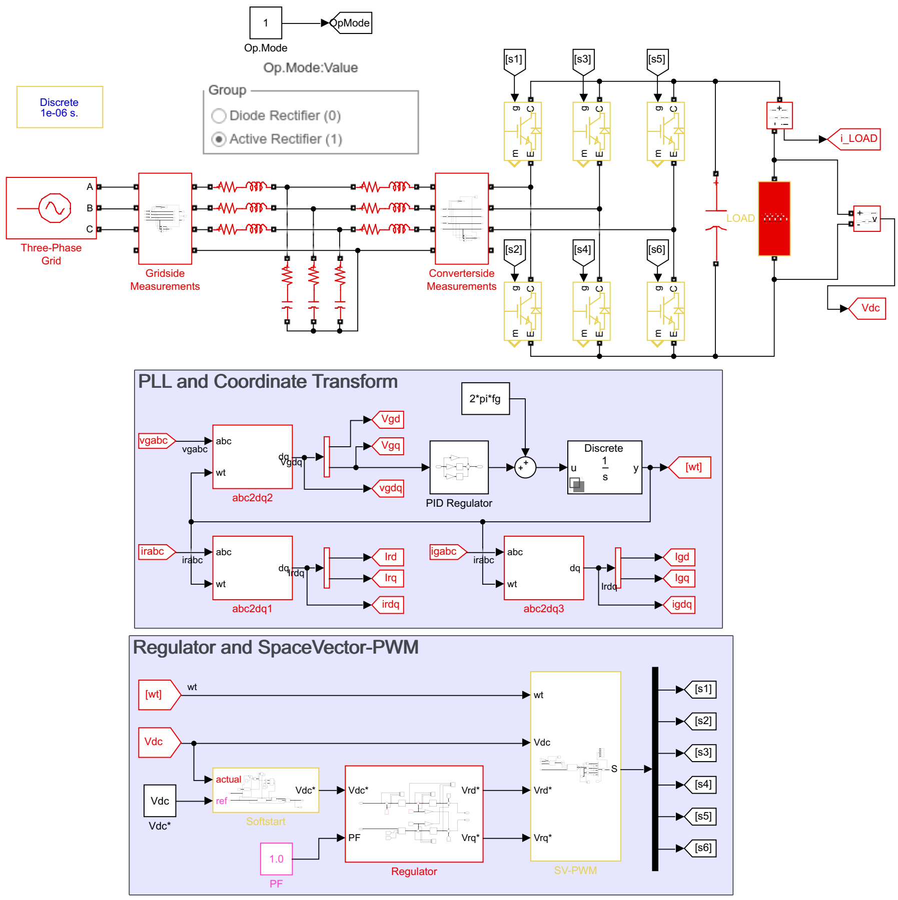

Figure 4.1: Simulink model overview.

with regulate for any variations on the load side. Simulations are conducted in order to observe the controller's response and performance during sudden changes in the load. To focus on the models response to load distubances, the simulation may be started from steady-state with the bulk capacitor charged and all transients died out. If starting the simulation from standstill with 0V on the DC-bus, some precaution must be taken; going immediately from 0V to steady-state will require a massive current transient in order to charge the large bulk capacitor. This will certainly trigger the fuses protecting the circuit in a real-life implementation, if not outright destroy the power transistors or other components. To start from standstill a hardware current limiter or a software softstarter must be considered. For use in this thesis, a software variant is implemented. It is also useful to introduce a saturation on the integrators of the PI-controllers, preventing integrator wind-up and big spikes in current from large sudden changes in the load.

Simulation parameters are loaded into MATLAB workspace from a .m MATLAB code file. This .m-file will both load predetermined parameters and calculate others, such as current control loop PI-gains, based on the conclusions reached in Chapter 3 Design. All parameter values are presented in Table 4.1 and Table 4.2.

Parameter	**Symbol**	**Value**	**Unit**
Rated Power	P_{LOAD}	2	kW
Grid Line Voltage	V_{LL}	400	V
DC Voltage Reference	V_{dc}	600	V
Grid Frequency	f_g	50	Hz
Switching Frequency	f_s	10	kHz
Grid-side Resistance	R_g	10	mΩ
Grid-side Inductance	L_g	2	mH
Rectifier Resistance	R_r	10	mΩ
Rectifier Inductance	L_r	2	mH
Filter Capacitor	C_f	2	μF
Capacitor esr	R_c	0	mΩ
DC-bus Capacitor	C_{dc}	1525	μF
Load Resistance	R_{LOAD}	180	Ω

Table 4.1: Simulation parameters.

Regulator	**kp**	**ki**	**kd**
Current	21.7556	79066	0
Voltage	1	150	0
PLL	10	5000	0

Table 4.2: PI parameter gains.

Chapter 5

Prototype

5.1 Cards and Components

5.1.1 Digital Signal Processor

LAUNCHXL-F28379D. The TMS320F2837xD is a powerful 32-bit floating point MCU designed for advanced closed-loop control applications [cite appendix LaunchPad datasheet].

CPU

The F2837xD supports a dual-core C28x Central Processing Unit (CPU) capable of providing 200 MHz of signal processing power in each core. Further enhancing the C28x CPUs is the trigonometric math unit (TMU) which enables efficient execution of trigonometric and arithmetic operations commonly found in control system applications. This dramatically increases the performance of trigonometric functions, whichs would otherwise be very cycle intensive.

GPIO

By default, all the pins on the board are configured as General-Purpose Input/Output (GPIO), and the GPIOs pins are inputs by default.

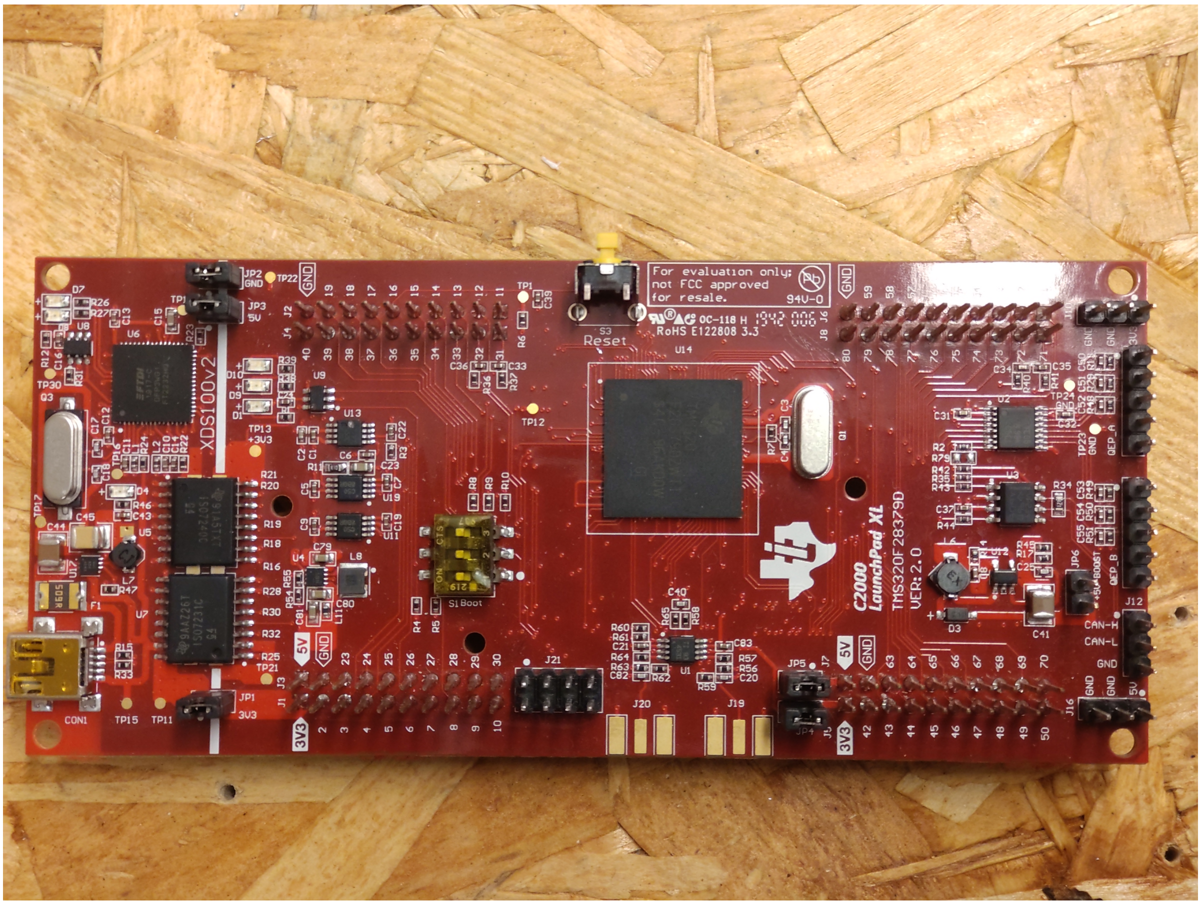

Figure 5.1: Launchpad.

Interrupt

In digital computers, an interrupt is a response by the processor to an event that needs attention from the software.When an interrupt request from either software or hardware is detected, the processor halts the current thread execution. The thread state is saved allowing the function called by the interrupt to be executed before resuming the halted thread where it left off. In real-time computing, interrupts are especially useful as they allow hardware devices indicating electronic or physical state changes to recive immediate attention.
The LAUNCHXL-F28379D has a peripheral interrupt expansion module capable of multiplexing up to sixteen peripheral interrupts into each of its twilve CPU interrupt lines. This adds up to support for 192 peripheral interrupt signals. The CPU can be configured to service one interrupt while others remain pending by using a series of flag and enable registers. The interrupt with the highest priority is executed.

Five external interrupts (XINT1 to XINT5) can be mapped onto any of the GPIO pins. These are especially useful for reading sensors or monitoring user input. Using an interrupt can ensure that the MCU catches the input while still performing its other tasks. The external interrupts have a timing requirement of minimum two cycles of the system clock; one cylcles is $t_{clockcycle} = \frac{1}{systemfrequency}$. From the datasheet the min/max system frequency is 2/200MHz resulting in a min/max clock cycle of 5/500ns. This translates to the external interrupt signal having to last for $2 \cdot 500ns = 1\mu s$ in the worst case.

ePWM

ADC

5.1.2 Control Board

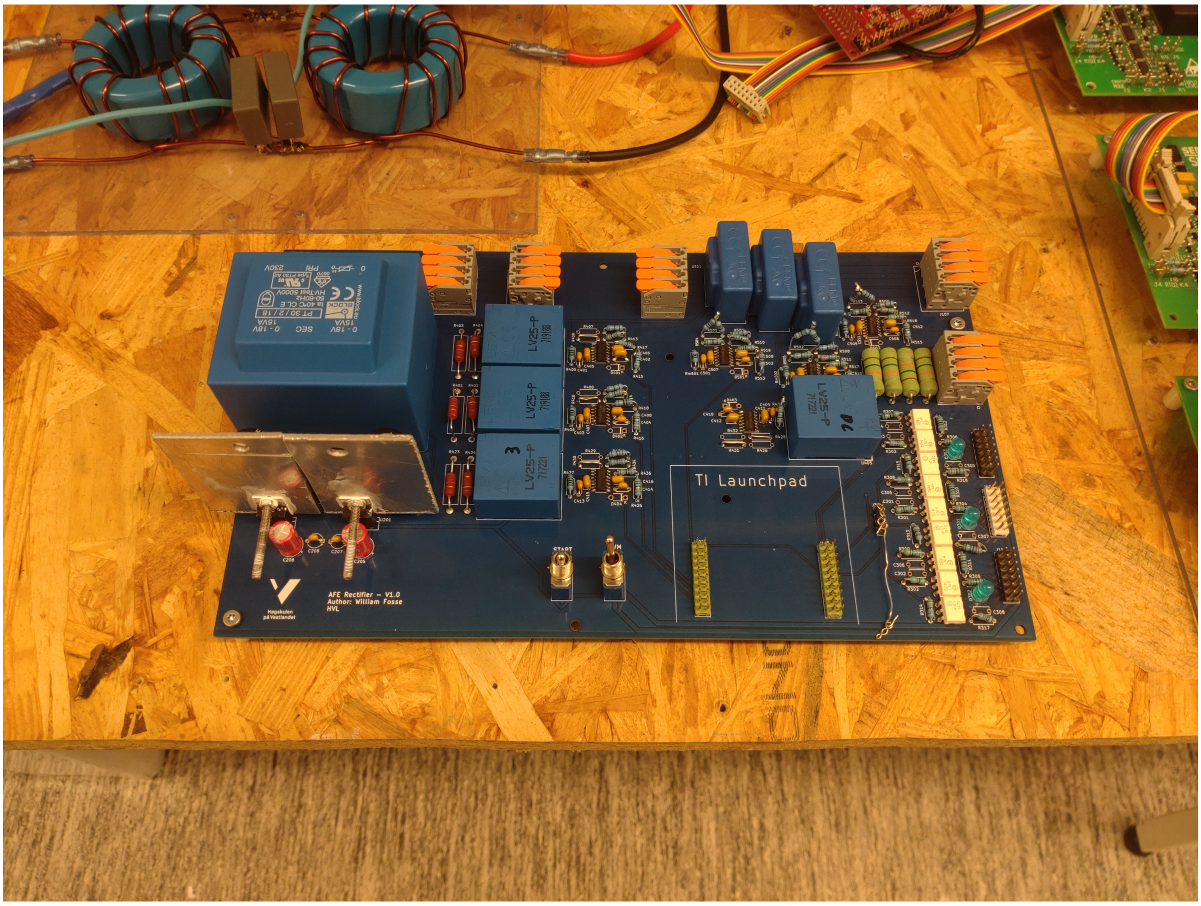

Figure 5.2: Control board.

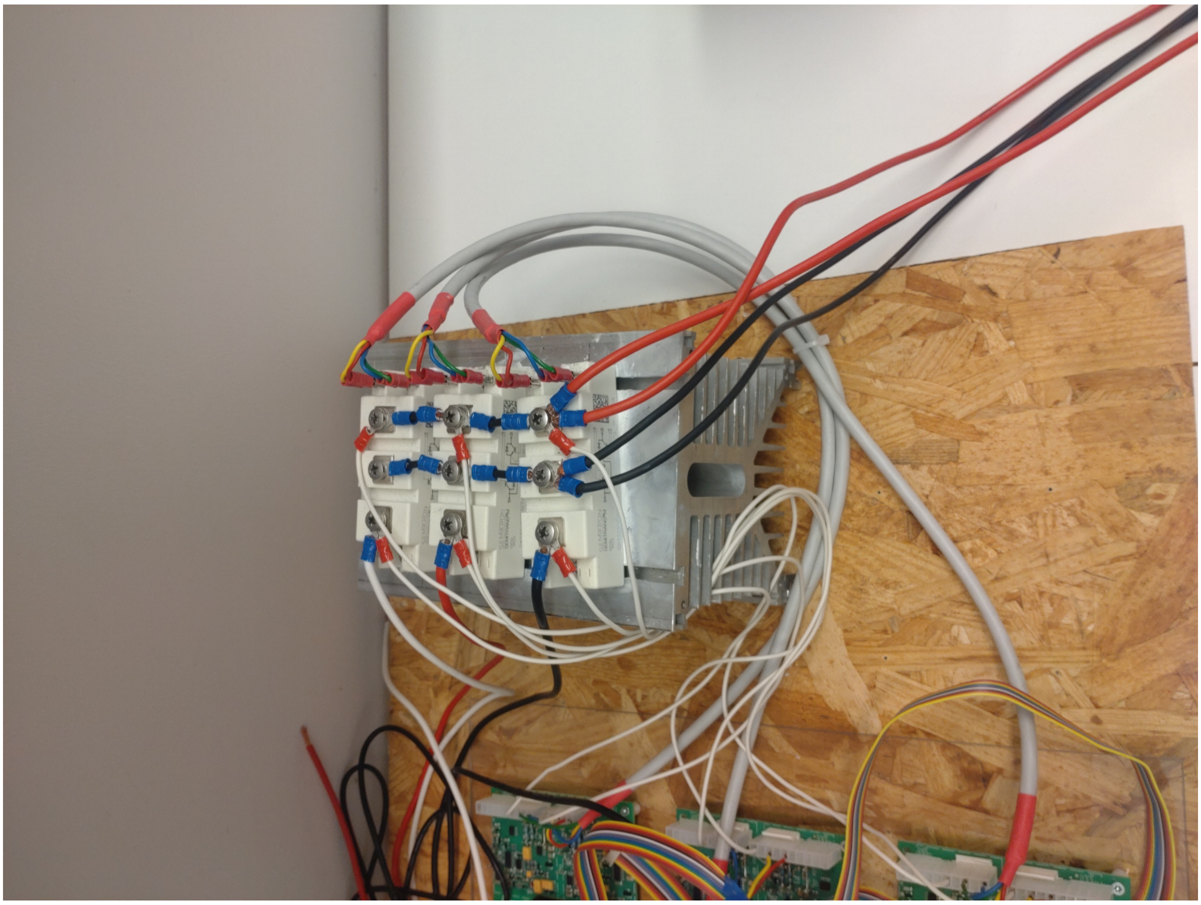

Figure 5.3: IGBT bridge on the heat sink.

5.1.3 IGBT Bridge

5.1.4 IGBT Driver Cards

5.1.5 LCL-Filter

5.1.6 Complete Model

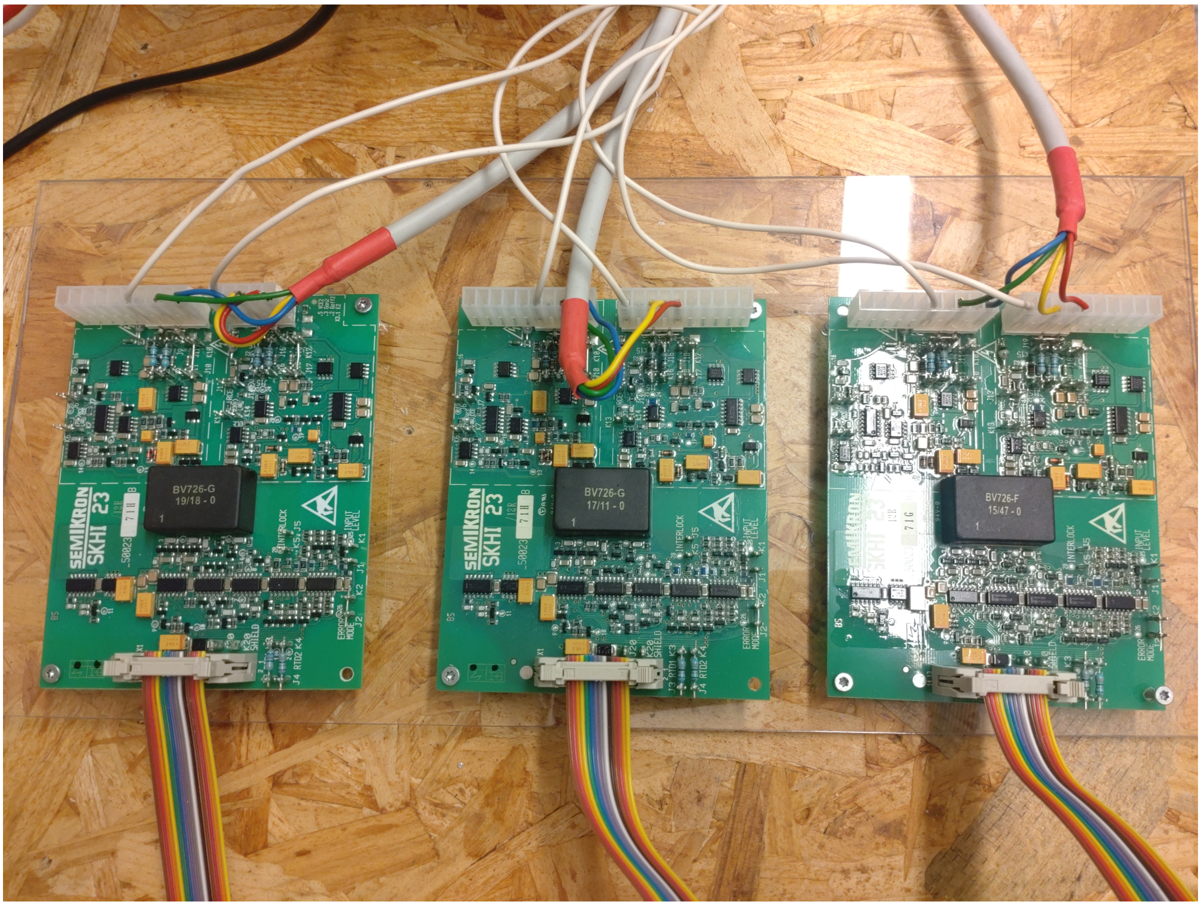

Figure 5.4: IGBT driver cards.

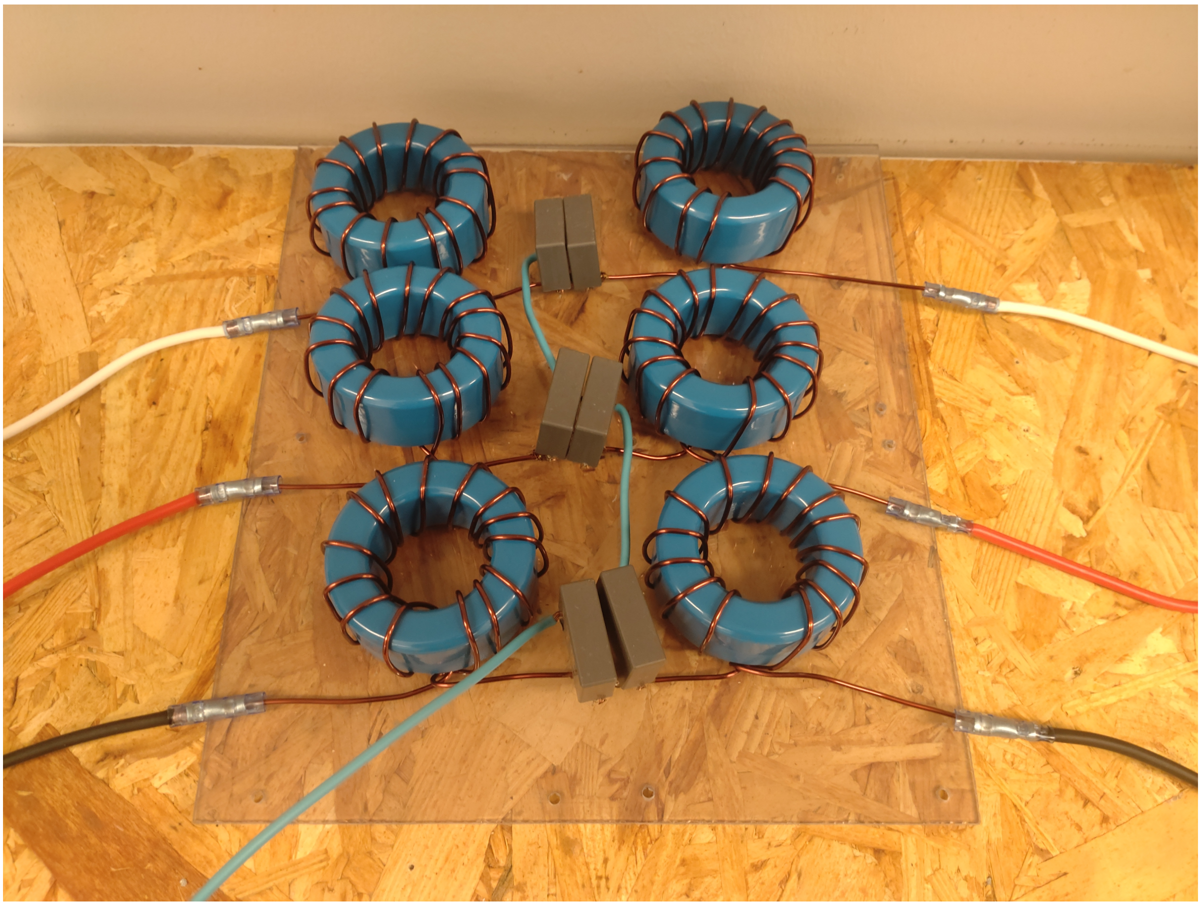

Figure 5.5: LCL filter.

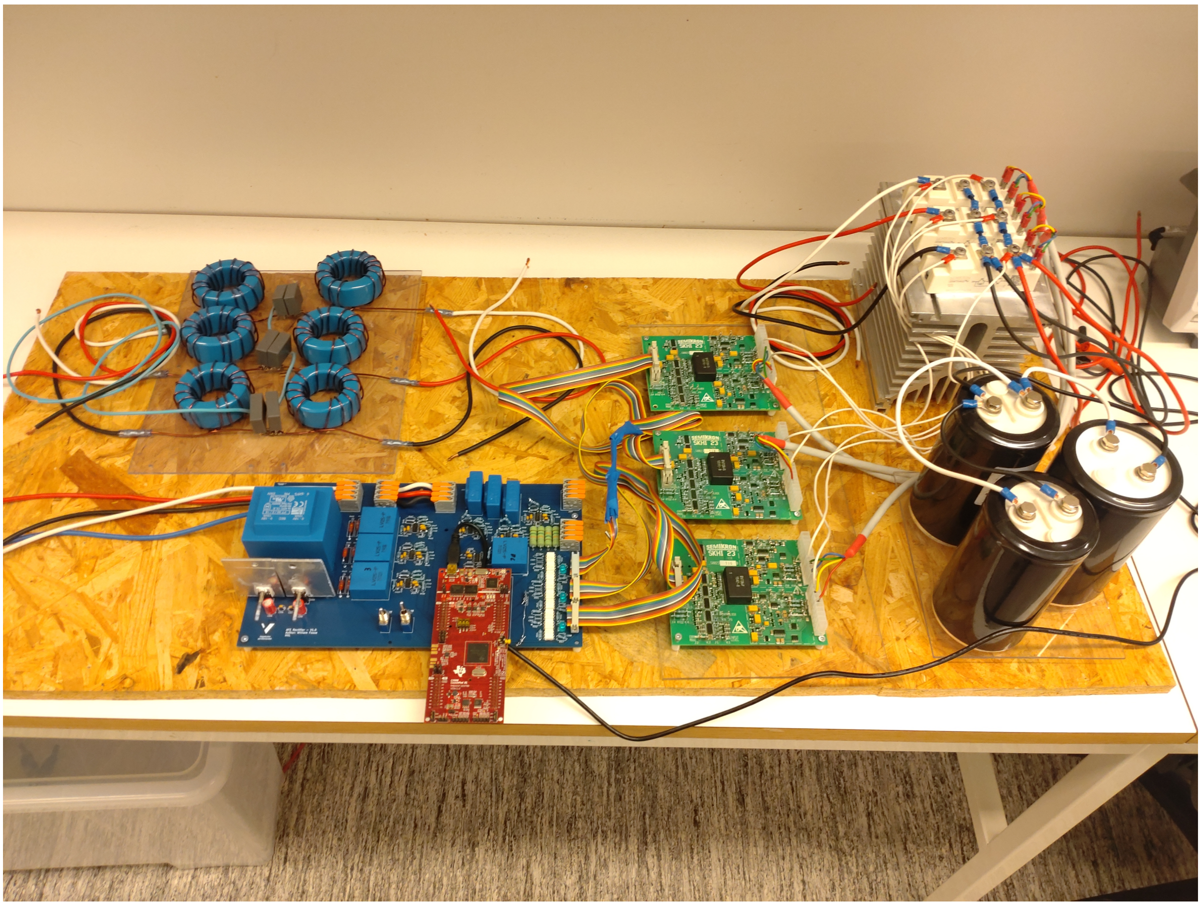

Figure 5.6: Complete model.

Chapter 6

Tests and Results

6.1 Simulation Results

In this section, simulation data will be presented. Some key parameters will be highlighted in relation to the applied load: Settling time T_s and voltage drop ΔV for the transients, and peak-to-peak DC voltage ripple v_{rip}, total harmonic current distortion THD_i and power factor PF for the steady-state. All simulations are starting from initial steady-state before a load increase or decrease is applied. Three different modes of operation will be tested: rectification, invertion and alternating bidirectional operation. The testing results are read by Simulink scopes. The recorded grid voltage and current is fed into the Simulink Power Systems "powergui" block's integrated Fast Fourier Transform (FFT) analysis function to measure THD.

6.1.1 Rectifier Operation

The load is a purely resistive at the rated value. Every 0.1s an ideal switch adds another equal resistive load in parallell.

6.1.2 Inverter Operation

The load consists of a nominal resistor load in series with a DC voltage source equal to two times the desired DC voltage. This serves to simulate a scenario in which an equal to nominal but opposite current is flowing back to the grid. Every 0.1s a series of ideal switches as series voltage sources increasing the inverting load in equal nomi-

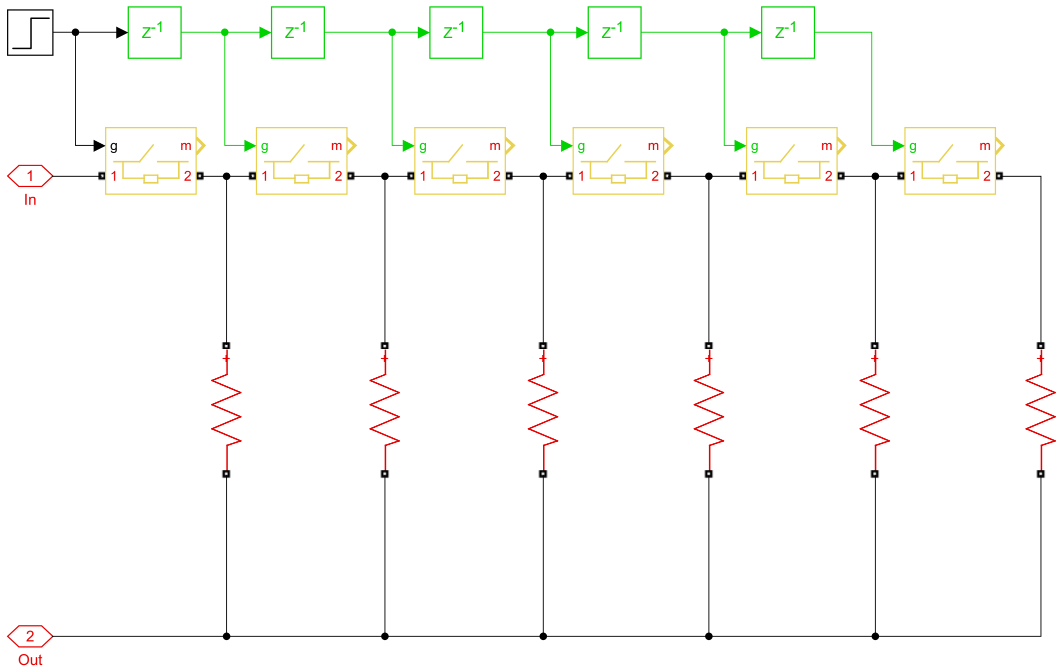

Figure 6.1: Blockdiagram of load for rectifier operation.

		Transient		Steady-State		
$T[s]$	$P[kW]$	$T_s[ms]$	$\Delta V[V]$	$v_{rip}[mV]$	$THD_i[\%]$	$PF[\%]$
$0 < t < 0.1$	2	24	3.5	40	3.38	1.0
$0.1 < t < 0.2$	4	24	3.5	50	1.70	1.0
$0.2 < t < 0.3$	6	25	3.5	80	1.12	1.0
$0.3 < t < 0.4$	8	28	3.5	100	0.83	1.0
$0.4 < t < 0.5$	10	26	3.5	125	0.70	1.0

Table 6.1: Transient and steady-state response during rectifier operation.

nal increments (except for a mistake in the implementation that doubles the first step increase).

6.1.3 Bidirectional Operation

The bidirectional load is a combination of the previous two resulting in increasingly large steps in load increase and decrease. This is the ultimate stress test of the proposed control system.

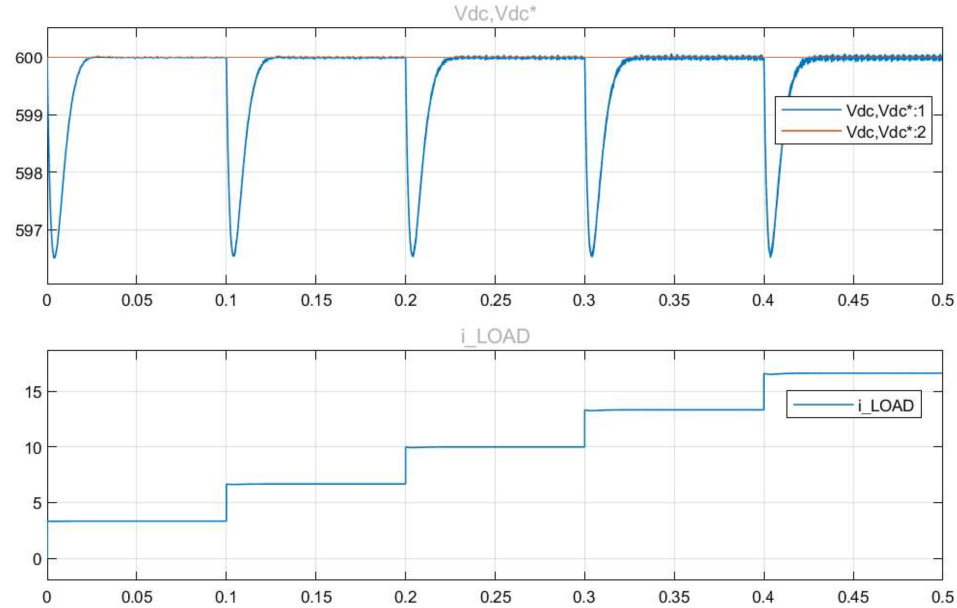

Figure 6.2: Plotted system response under rectifier operation.

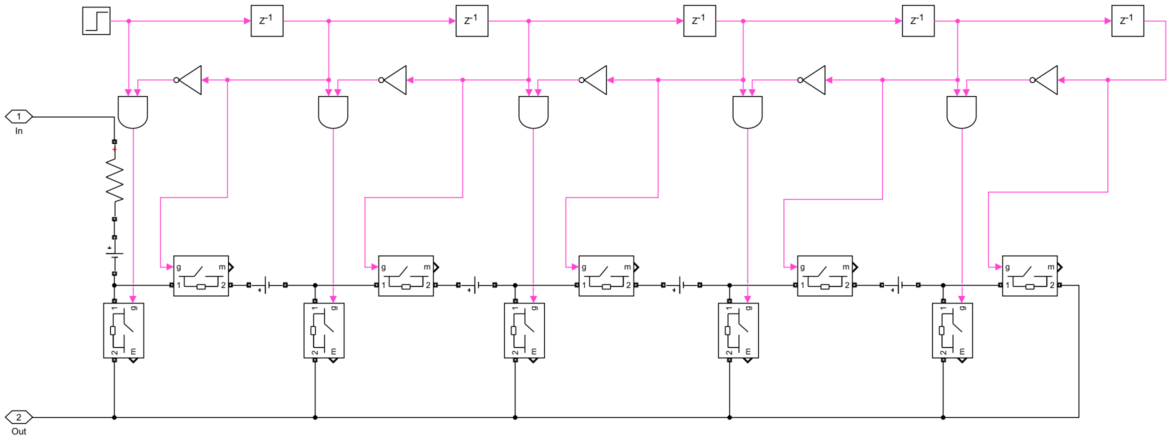

Figure 6.3: Blockdiagram of load for inverter operation.

		Transient		Steady-State		
$T[s]$	$P[kW]$	$T_s[ms]$	$\Delta V[V]$	$v_{rip}[mV]$	$THD_i[\%]$	$PF[\%]$
$0 < t < 0.1$	-2	23	-3.45	40	3.32	-1.0
$0.1 < t < 0.2$	-6	23	-6.9	65	1.16	-1.0
$0.2 < t < 0.3$	-8	24	-3.5	100	0.85	-1.0
$0.3 < t < 0.4$	-10	24	-3.5	120	0.71	-1.0
$0.4 < t < 0.5$	-12	24	-3.5	140	0.55	-1.0

Table 6.2: Transient and steady-state response during inverter operation.

		Transient		Steady-State		
$T[s]$	$P[kW]$	$T_s[ms]$	$\Delta V[V]$	$v_{rip}[mV]$	$THD_i[\%]$	PF
$0 < t < 0.1$	2	24	3.5	40	3.29	1.0
$0.1 < t < 0.2$	-2	33	-6.8	40	3.40	-1.0
$0.2 < t < 0.3$	4	24	10.5	60	1.70	1.0
$0.3 < t < 0.4$	-4	33	-13.5	60	1.75	-1.0
$0.4 < t < 0.5$	6	28	17.0	80	1.18	1.0

Table 6.3: Transient and steady-state response during bidirectional operation.

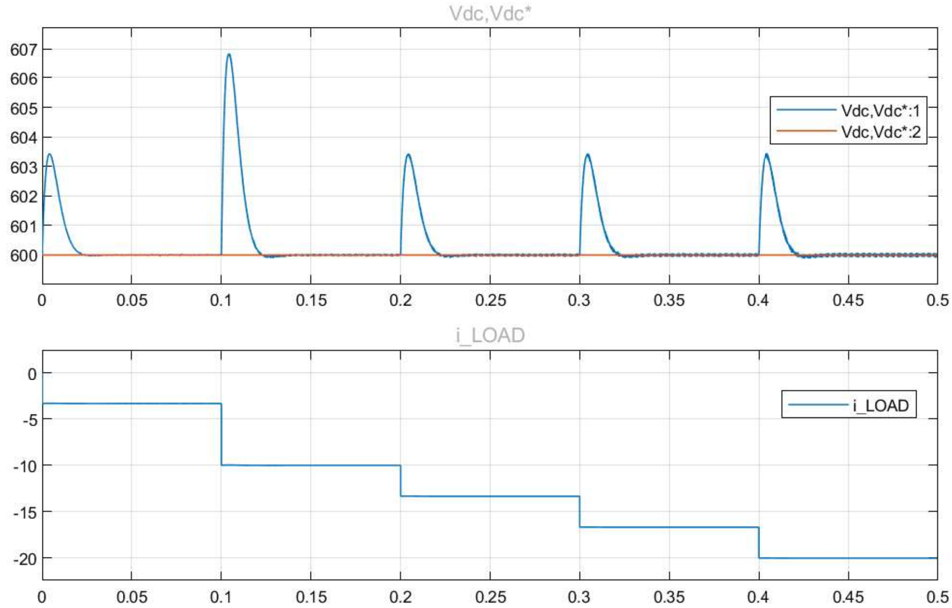

Figure 6.4: Plotted system response under inverter load conditions.

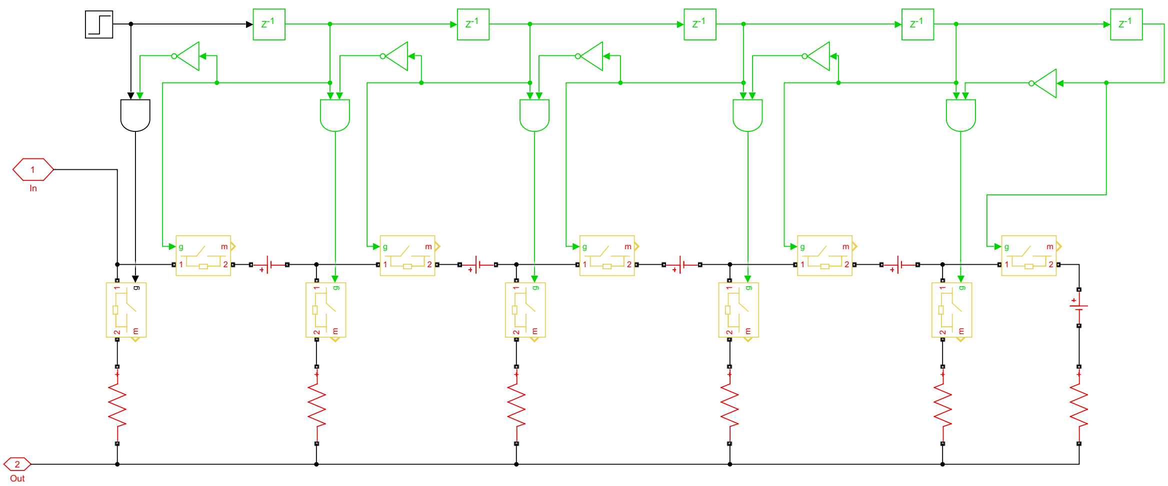

Figure 6.5: Blockdiagram of load for bidirectional operation.

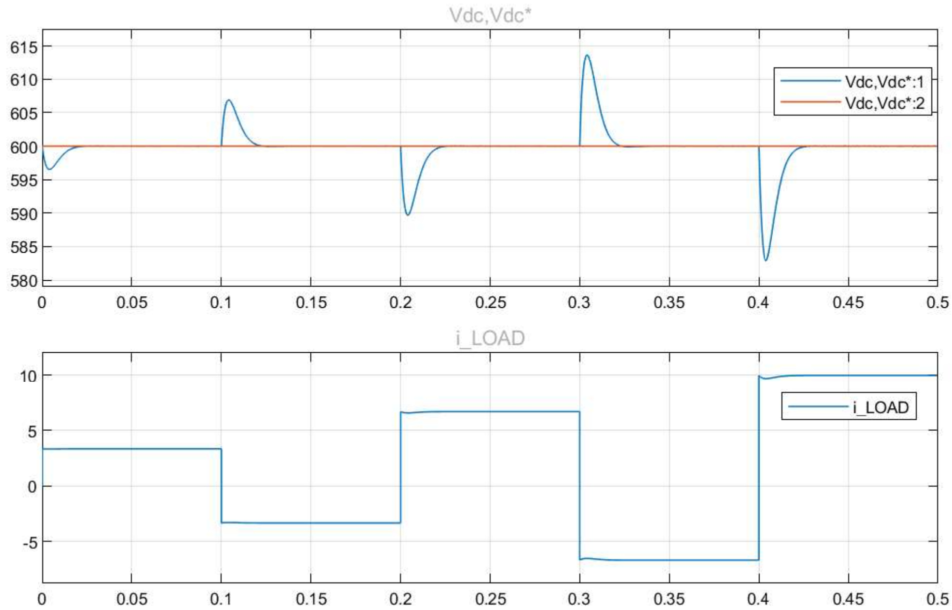

Figure 6.6: Plotted system response under bidirectional load operation.

Chapter 7

Discussion and Conclusion

This thesis aimed to design and control a 2 kW three-phase rectifier with bidirectional functionality for EV charger applications. A system structure was proposed by considering appropriate rectifier systems and control schemes. The proposal consists of an AFE rectifier topology, and a VOC based control scheme. The rectifier bridge consists of six IGBTs, whose gate signals are generated by a SV-PWM switching scheme. A PLL algorithm extracts the phase angle of the grid voltage and synchronizes the switching of the rectifier. An LCL-filter forms a buffer between the grid and the rectifier bridge to filter out switching noise. A mathematical model of the system was presented and modelled in Simulink. Simulations were conducted to investigate the performance of the system. Tests subjected the system to increasing step loads during rectifying, inverting and bidirectional operation. The transient and steady state responses of the contoller were recorded. An FFT analysis was also conducted for each load instance to observe the level of harmonic distortion.

The results of the simulations indicate that the system is capable of bidirectional current flow. Furthermore, the controller is able to maintain a stable DC voltage og 600 V during several multiples of nominal load conditions with minimal transient voltage drop. UPF is reached during rectification, and it is reached during inversion with a leading Power Factor (PF). The LCL-filter is shown to be able to attenuate the current harmonics to an acceptable level adhering to IEEE standards. According to the results, voltage ripple of the transient response of the controller deteriorates during off-nominal conditions, i.e. it increases. THD_i however seems to improve with increasing load suggesting that the controller might be sub-optimally tuned.

An experimental prototype was thoroughly designed and built for the purpose of confirming the simulated results. Some tests were conducted but however not recorded, thus further testing is required in order to conclude if the system is appropriate for implementation.

Bibliography

[1] A. C. Bøeng, "Fakta om energi - Utviklingen i energibruk i Norge," *Statistisk sentralbyrå (sbb.no)*, p. 14, Mar. 2013. 1.1

[2] UNFCCC, "The Paris Agreement," in *Paris Climate Change Conference - November 2015*, Nov. 2018. 1.1

[3] "Statistikk elbil." https://elbil.no/om-elbil/elbilstatistikk/, 2022. 1.1

[4] "IEEE Standard for Harmonic Control in Electric Power Systems," *IEEE Std 519-2022 (Revision of IEEE Std 519-2014)*, pp. 1–31, Aug. 2022. 1.2

[5] "IEEE Standard for Interconnection and Interoperability of Distributed Energy Resources with Associated Electric Power Systems Interfaces," *IEEE Std 1547-2018 (Revision of IEEE Std 1547-2003)*, pp. 1–138, Apr. 2018. 1.2

[6] "IEEE Standard for Technical Specifications of a DC Quick and Bidirectional Charger for Use with Electric Vehicles," *IEEE Std 2030.1.1-2021 (Revision of IEEE Std 2030.1.1-2015)*, pp. 1–147, Feb. 2022. 1.2

[7] N. Mohan, *Power Electronics: Converters, Applications, and Design.* Wiley, third ed., Nov. 2002. 2.1, 2.1

[8] J. Lutz, H. Schlangenotto, U. Scheuermann, and R. De Doncker, *Semiconductor Power Devices: Physics, Characteristics, Reliability.* Berlin, Heidelberg: Springer, 2011. 2.1, 7

[9] N. Mohan, *Advanced Electric Drives: Analysis, Control, and Modeling Using MATLAB / Simulink.* Wiley, Aug. 2014. 2.3.2

[10] M. B. Said-Romdhane, M. W. Naouar, I. S. Belkhodja, and E. Monmasson, "An Improved LCL Filter Design in Order to Ensure Stability without Damping and Despite Large Grid Impedance Variations," *Energies*, vol. 10, p. 336, Mar. 2017. 3.1

List of Figures

List of Tables

Glossary

commutation transfer of current between two conductors. 7

phototransistor semiconductor device where emitter-collector current is controlled by level of light received. 17

propagation the process by which a disturbance or signal, such as an electromagnetic wave, is transmitted through a medium. 17

Acronyms

AFE Active Front End. 7, 12, 30

BJT Bipolar Junction Transistor. 4

CPU Central Processing Unit. 21

DPC Direct Power Control. 12, 13

esr Equivalent Series Resistance. 14

FFT Fast Fourier Transform. 23, 30

GPIO General-Purpose Input/Output. 21

GTO Gate Turn-off Thyristor. 4

IEEE Institute of Elecrtical and Electronics Engineers. 2, 30

IGBT Insulated Gate Bipolar Transistor. 4, 8, 30, 33

LED Light Emitting Diode. 17

MCU Microcontroller Unit. 12, 17, 18, 21

MOSFET Metal-Oxide-Semiconductor Field Effect Transistor. 4

PCB Printed Circuit Board. 2

PF Power Factor. 30

PLL Phase-Locked Loop. 17, 18

PWM Pulse-Width-Modulation. 12

rms root-mean-square. 6

S-PWM Sinusoidal Pulse-Width-Modulation. 12

SV-PWM Space-Vector Pulse-Width-Modulation. 12, 18, 30

THD Total Harmonic Distortion. 2, 12, 13, 23, 30

UPF Unity Power Factor. 18, 30

VOC Voltage Oriented Control. 12, 13, 30

Appendix A

Schematics

A.1 Main Wiring Diagram

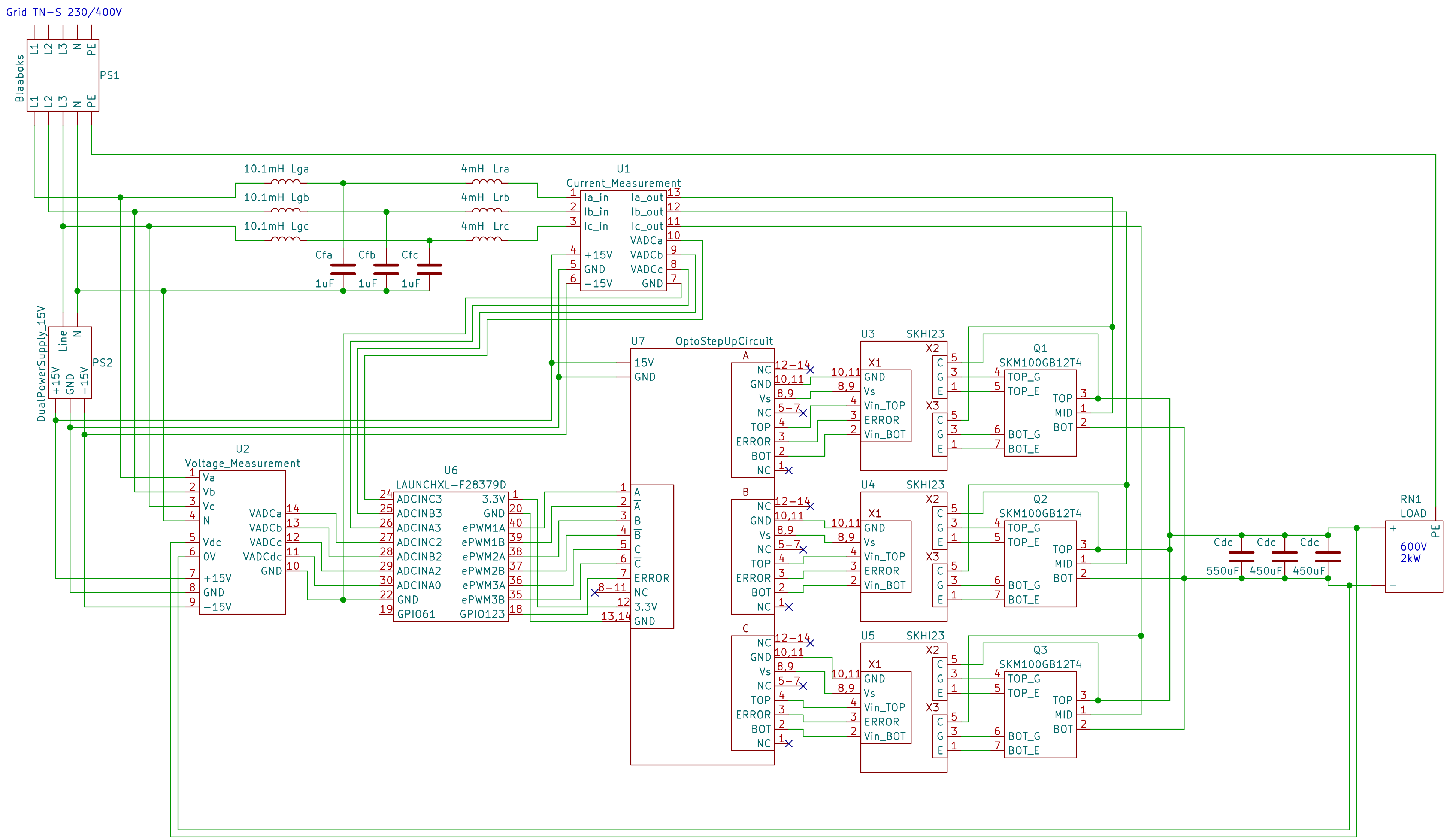

Author: William Fosse
Masterprosjekt Energi/Elkraftteknikk
HVL
Sheet: /
File: GridTiedAFE.kicad_sch

Title: AFE Rectifier Wiring Diagram

Size: A4 | Date: 2022-05-09 | **Rev: V1.0**
KiCad E.D.A. kicad (6.0.4) | Id: 1/1

A.2 Control Board Schematic

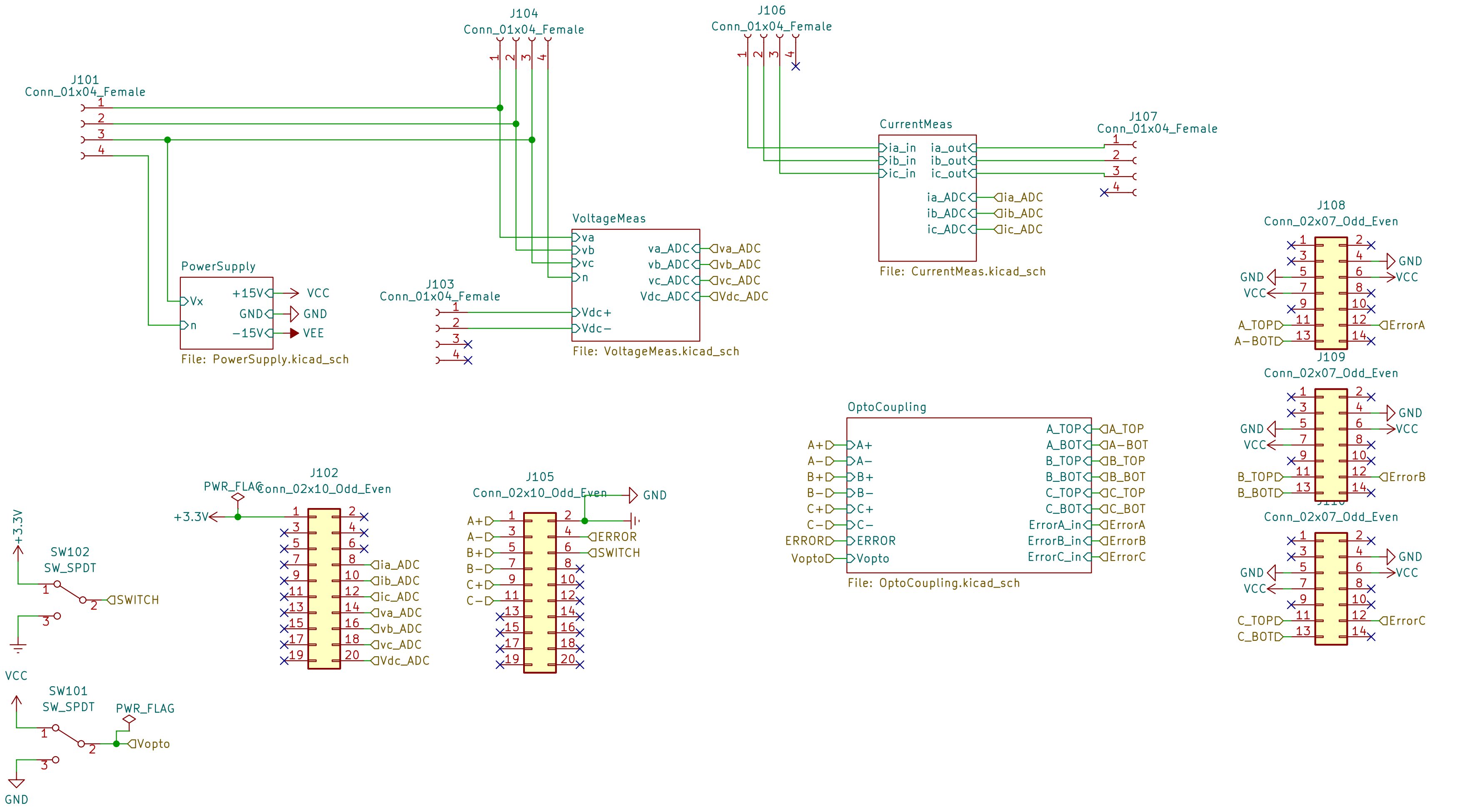

Author: William Fosse

Masterprosjekt Energi/Elkraftteknikk

HVL

Sheet: /

File: AFE_ControlBoard.kicad_sch

Title: ActiveFrontEndRectifierControlBoard

Size: A4 | Date: 2022-05-09 | **Rev: V1.0**

KiCad E.D.A. kicad (6.0.4) | Id: 1/5

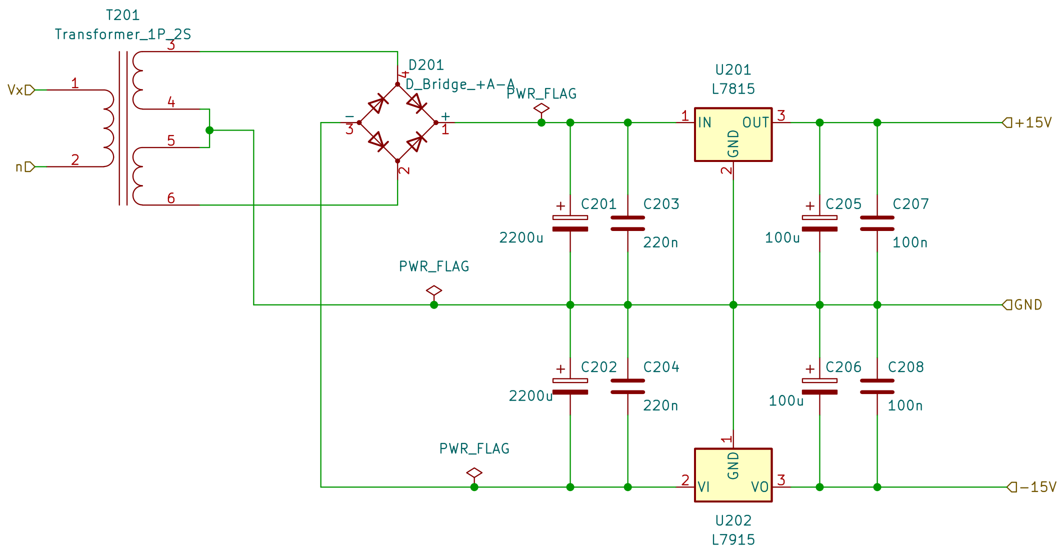

Author: William Fosse
Masterprosjekt Energi/Elkraftteknikk
HVL

Sheet: /PowerSupply/
File: PowerSupply.kicad_sch

Title: ActiveFrontEndRectifierControlBoard

Size: A4	Date: 2022-05-09	**Rev: V1.0**
KiCad E.D.A. kicad (6.0.4)		Id: 2/5

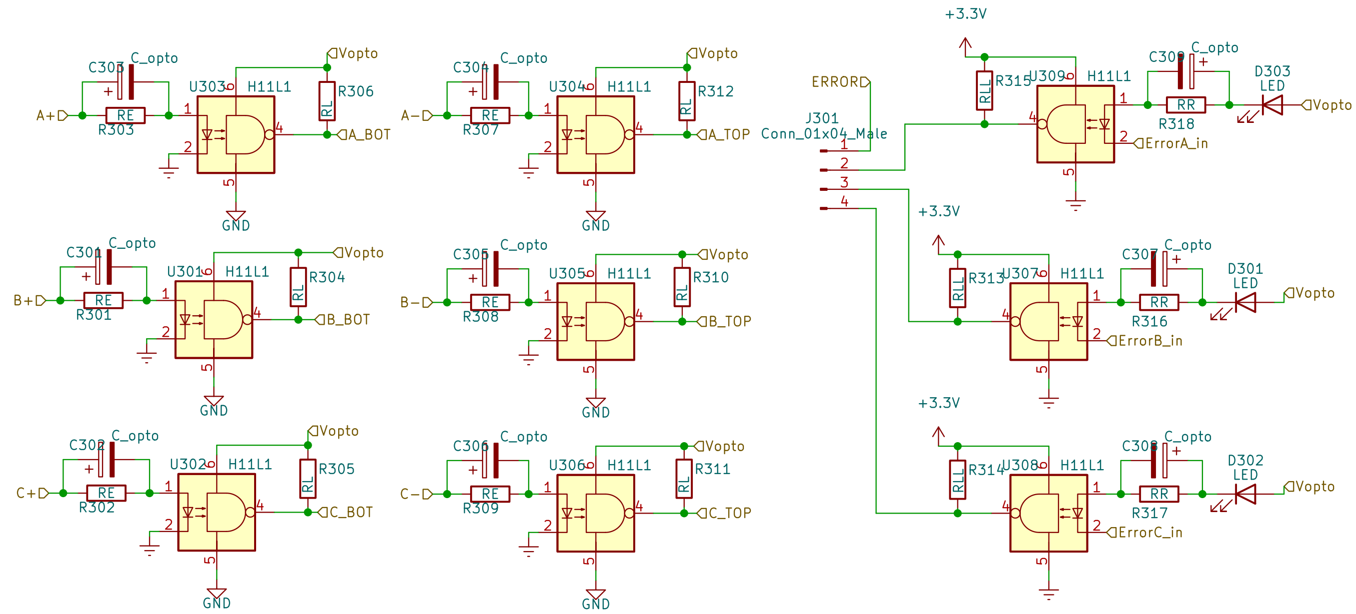

Author: William Fosse
Masterprosjekt Energi/Elkraftteknikk
HVL

Sheet: /OptoCoupling/
File: OptoCoupling.kicad_sch

Title: ActiveFrontEndRectifierControlBoard

Size: A4 | Date: 2022-05-09 | **Rev: V1.0**
KiCad E.D.A. kicad (6.0.4) | Id: 3/5

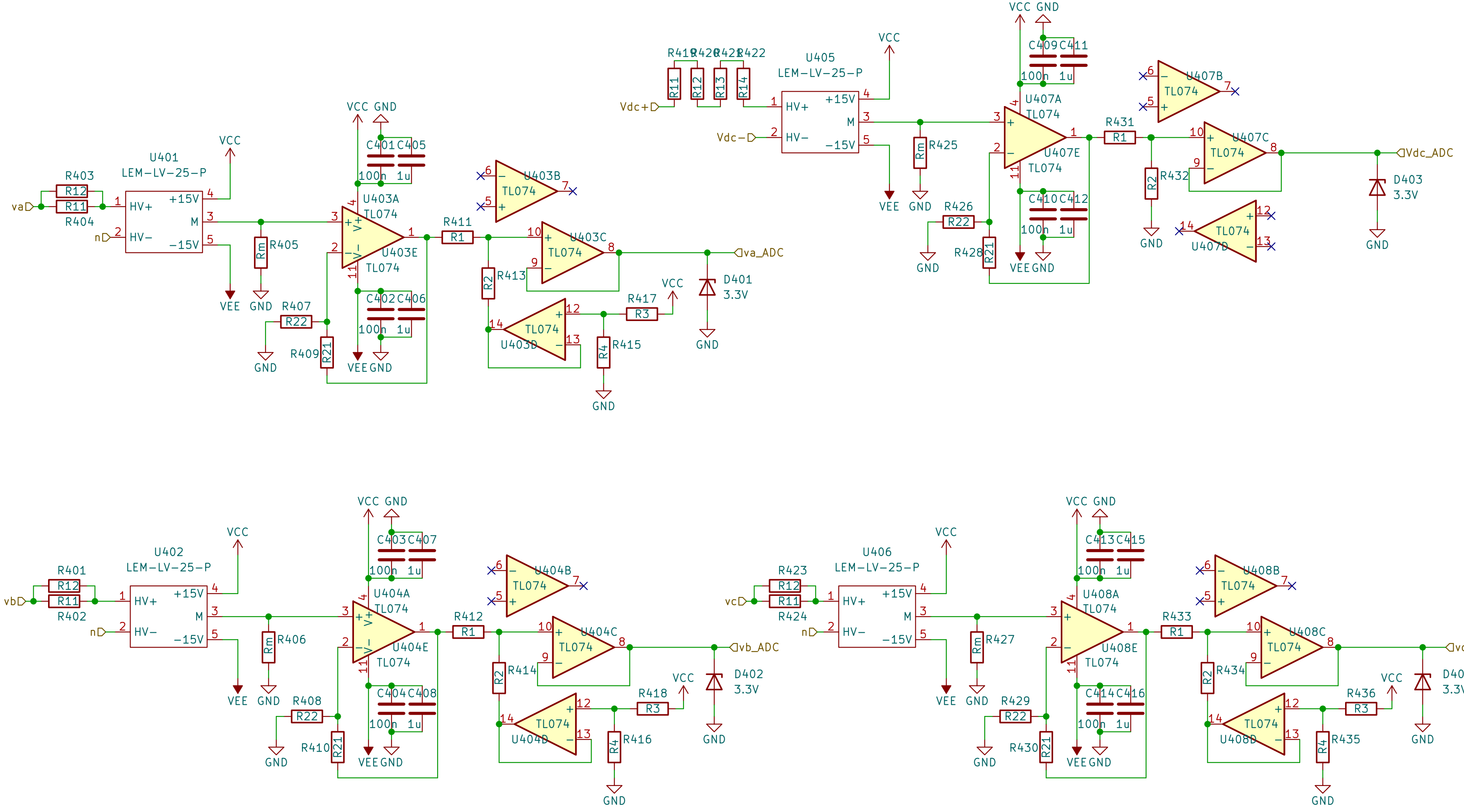

Author: William Fosse
Masterprosjekt Energi/Elkraftteknikk
HVL

Sheet: /VoltageMeas/
File: VoltageMeas.kicad_sch

Title: ActiveFrontEndRectifierControlBoard

Size: A4 Date: 2022-05-09 **Rev: V1.0**
KiCad E.D.A. kicad (6.0.4) Id: 4/5

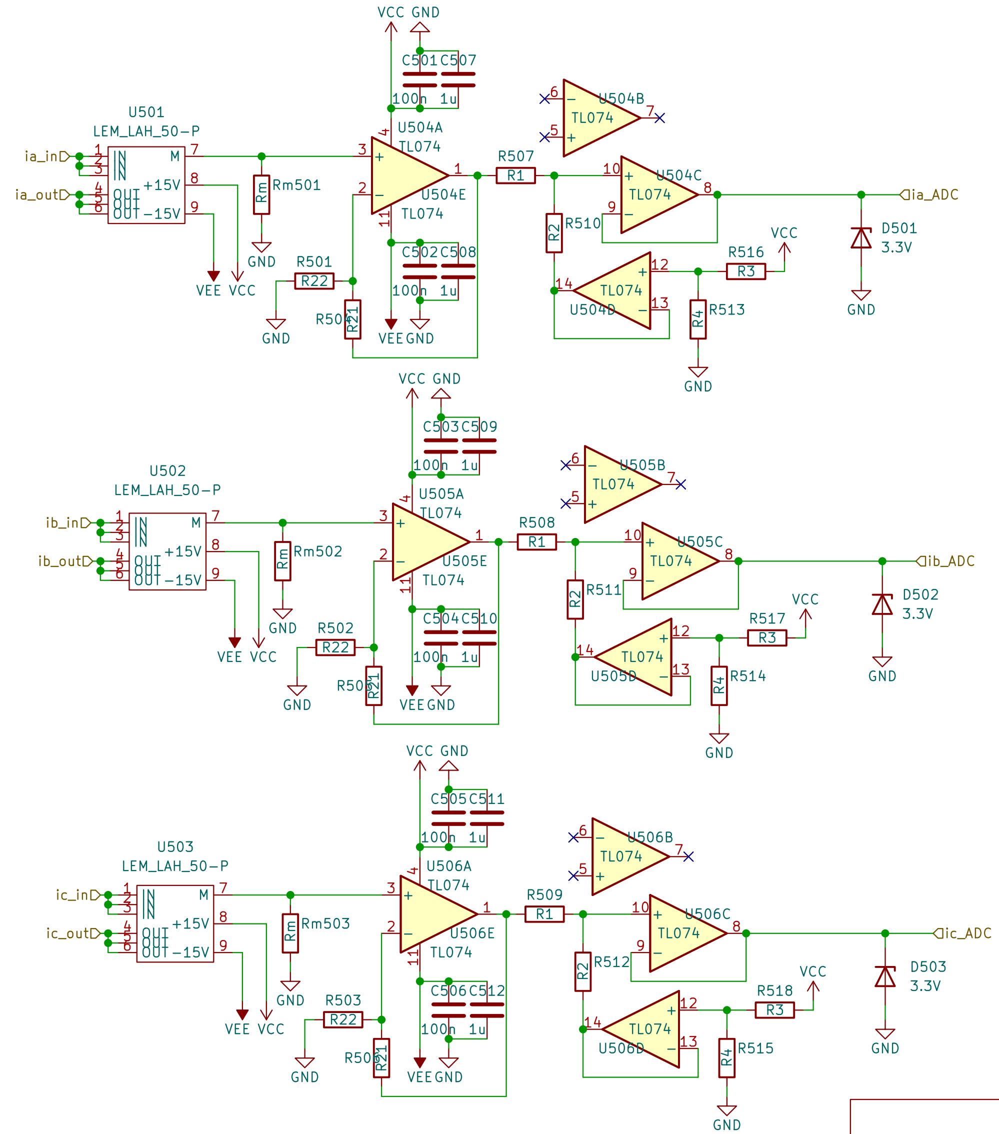

Author: William Fosse
Masterprosjekt Energi/Elkraftteknikk
HVL

Sheet: /CurrentMeas/
File: CurrentMeas.kicad_sch

Title: ActiveFrontEndRectifierControlBoard

Size: A4 | Date: 2022-05-09 | Rev: V1.0
KiCad E.D.A. kicad (6.0.4) | Id: 5/5

Appendix B

MATLAB Code

B.1 Coordinate Transform

B.1.1 abc2$\alpha\beta$

```
function [alpha, beta] = abc2ab(a, b, c)
alpha = (2*a-b-c) * 1/sqrt(6);
beta = (b-c)*1/sqrt(2); % se paa meg
```

B.1.2 $\alpha\beta$2dq

```
function [d, q] = ab2dq(alpha, beta, wt)
d = alpha*sin(wt) - beta*cos(wt);
q = alpha*cos(wt) + beta*sin(wt);
```

B.1.3 dq2$\alpha\beta$

```
function [alpha, beta] = dq2ab(d, q, wt)
alpha = d*sin(wt) + q*cos(wt);
beta = -d*cos(wt) + q*sin(wt);
```

B.1.4 $\alpha\beta$2abc

```
function [a, b, c] = ab2abc(alpha, beta)
a=sqrt(2/3)*alpha;
b=sqrt(2/3)*((-0.5)*alpha+(sqrt(3)/2)*beta);
c=sqrt(2/3)*((-0.5)*alpha+(-sqrt(3)/2)*beta);
```

Appendix C

Attachments

- TI LaunchPad LAUNCHXL-F28379D Overview
- TI TMS320x2833x, TMS320x2823x Technical Reference Manual
- TI TMS320F2837xD Dual-Core Microcontollers Datasheet
- IEEE Standard Technical Specifications of a DC Quick Charger for Use with Electric Vehicles
- IGBT Module SKM100GB12T4 Datasheet
- IGBT Driver Card SKHI23 Datasheet